POLITECNICO DI MILANO

Facoltà di Ingegneria Industriale

Corso di Laurea in Ingegneria Aeronautica

Energy and enstrophy balances for wall-bounded turbulent flows with drag reduction

Relatore: Prof. Maurizio Quadrio
Corelatore: Dr. Pierre Ricco

Tesi di Laurea di:
Claudio Ottonelli, matr. 712181

Anno Accademico 2009 – 2010

Acknowledgements

I would like to express my gratitude to the Department of Mechanical Engineering at King's College London for the hospitality from October 2009 until February 2010, in particular I would like to thank Dr Pierre Ricco for the cohabitation and his family for the patience demonstrated to us. I also thank Dr Andrea Ducci for the enlightening discussions on the enstrophy production in section §3.2.2.

Abstract

With the aim of understanding drag reduction mechanism on a turbulent channel flow, modified by in-plane sinusoidal oscillations of the walls, statistics of energy and enstrophy balances of the mean and fluctuating flow field obtained by direct numerical simulations, are studied. It is observed that as the bulk streamwise velocity increases and the intensity of the turbulent kinetic energy decreases due to the wall motion, the viscous dissipations associated with both the mean flow and the turbulent fluctuations increases. Through energy and enstrophy balances, it is found that the spanwise oscillating shear acts strongly on the turbulent dissipation, which is suitably represented by the turbulent enstrophy. Turbulent vorticity lines in planes perpendicular to the streamwise direction are stretched by the large-scale spanwise forcing, which is evidenced by flow visualizations and elucidated by a simple dynamical model. The study of enstrophy production allows extracting a parameter useful for predicting drag reduction. The present approach may be readily extended to other turbulent flows forced at large scale to unravel the physical mechanisms.

Keywords: Turbulent wall flows, Drag rduction, Spanwise-oscillating wall forcing, Enstrophy

Sommario

Con l'obiettivo di capire il meccanismo di riduzione d'attrito con un approccio statistico, i bilanci di energia ed enstrofia dei campi di flusso medio e turbolento sono studiati per il caso di un canale piano indefinito, forzato da un'oscillazione sinusoidale della parete in direzione trasversale, mediante DNS. Viene quindi condotta un'analisi di tipo statistico sulle caratteristiche principali del flusso medio e del flusso turbolento. Con l'aumento dell'energia cinetica e la diminuzione dell'intensità dell'energia cinetica turbolenta, a causa dell'azione della parete, la dissipazione viscosa associata alle fluttuazioni turbolente aumenta. Con l'ausilio dei bilanci di energia ed enstrofia, si trova che l'azione trasversale agisce fortemente sulla dissipazione turbolenta, che può essere in alternativa rappresentata dall'enstrofia turbolenta. Le visualizzazioni del campo di moto evidenziano il comportamento delle linee vorticose che vengono stirate e deviate dall'azione della forzante trasversale. Lo studio della produzione di enstrofia permette di evidenziare un termine che può essere legato linearmente alla riduzione d'attrito e ricavare un modello utile per la sua predizione. Il presente approccio può essere esteso ad altri flussi turbolenti forzati su grande scala per rivelarne il meccanismo fisico alla base della riduzione d'attrito.

Parole chiave: Flussi turbolenti di parete, Riduzione d'attrito, Parete oscillante, Enstrofia

Contents

List of Figures

Chapter 1

Introduction

An introduction to turbulent drag reduction and the related open questions is outlined in this chapter. In order to set the stage for the present work, a brief review of the main flow control techniques is presented, and the plain channel flow considered throughout this work is introduced.

1.1 Turbulent flow and drag reduction

The reduction of the skin-friction drag in wall-bounded turbulent flows is one of the most challenging and important areas of fluid mechanics, due to economical and ecological interests in various industrial applications. The difficulty lies both in the extreme complexity of the physics underlying turbulent flows and in the resilience of such flows to favourably change when disturbed by external agents. In spite of the huge amount of experiments and numerical simulations, the physical process of drag reduction is still not satisfactorily understood, and some disagreements exist among researchers. As an example, let us consider the oscillating wall forcing on a turbulent channel flow, one of the most studied benchmark problems among active control systems. Due to Jung et al. (1992), the oscillating wall is one of the open-loop control system, based on the spanwise forcing of the wall with sinusoidal law, which gives a drag reduction rate of ~ 0.5. Even for this case there is not an exact solution of the problem, there is not a specific guideline whether using for the simulations a constant mass flow rate (Quadrio et al., 2009) or keeping the pressure gradient constant (Quadrio and Ricco, 2010). Results are often in contrast with previous studies, for example in some cases the root mean squared value of the fluctuating velocity components increase (Du and Karniadakis, 2000), while in other works an opposite behaviour is demonstrated (Quadrio and Ricco, 2010). The physical meaning and consequently the identification of some parameters describing drag reduction behaviour, is also not agreed upon among authors; for example, in Choi (2002) it is explained how the reduction of drag only depends on the forcing velocity amplitude and that the oscillating period is not important in the scaling process; this statement is confuted by Quadrio and Ricco (2004) in which a scaling model is proposed depending on both the amplitude and the oscillating period.

Channel flows with spanwise-wall oscillations have been studied extensively mainly

through turbulence statistics (Choi et al., 1998; Quadrio and Sibilla, 2000), flow visualizations of the near-wall modified flow (Quadrio and Ricco, 2003), and simplified models of turbulence (Dhanak and Si, 1999) to the end of explaining the physical mechanisms leading to drag reduction. Further efforts have been directed to the search for analytic formulas for drag reduction prediction (Choi et al., 2002). Despite decades of research, the fundamental questions of why a skin-friction coefficient reduction occurs and how wall-bounded flows can be modified most efficiently to achieve a global energy saving still remain elusive.

The interest in the subject is steadily growing as the viscous action exerted by turbulence is cause of dramatic energetic losses in flow systems of technological relevance, such as oil and gas pipelines, high-speed aircraft wings, jet engines intakes, and turbine blades. Even a small reduction of turbulence activity, and thus of wall friction, translates in an improved system efficiency and therefore in lower fuel consumption. Further advantages are the attenuation of noise, structural vibrations, and aerodynamic heating.

1.2 Turbulent flow control

During the past several decades a number of strategies to control the turbulence level in order to reduce the skin friction coefficient has been developed. A brief review of the principal control techniques is summarized in this section. The techniques currently under development are mainly active (i.e. require energy to work) and open-loop (no need for sensors), although a general description is also given for passive control techniques and closed-loop techniques. The approach used to evaluate a control algorithm concerns both the energetic efficiency and the effectiveness of the control technique. Following the notation proposed by Kasagi et al. (2009a), we define the drag reduction rate R as the reduction of power pumped into the system:

$$R = \frac{P_0 - P}{P_0}, \tag{1.1}$$

where the subscript 0 refers to the uncontrolled flow. A second parameter, the effectiveness of the control algorithm, related to the additional power required to enforce the control system P_{in}, reads as follows:

$$G = \frac{P_0 - P}{P_{in}}. \tag{1.2}$$

Finally, the third parameter is the net power saved rate S, defined as:

$$S = \frac{P_0 - (P + P_{in})}{P_0} \tag{1.3}$$

and represent the maximum energy saving rate achieved. These parameters are related each other and are chosen as the foundamental performance indices to evaluate a flow control scheme.

1.2.1 Passive techniques

Passive flow control techniques, for which there is no need of energy input, are mainly characterized by a non-smooth surface capable of interacting favourably with the flow. Even if potential drag reductions are not particularly large, they are under active study because of their appealing simplicity. A well referenced example is represented by riblets (Walsh, 1980), a surface with V-shaped protrusions (crests) directly applied on surfaces. They act on the wall cycle (Choi, 1989) stabilizing the quasi-streamwise-vortex structures. Although the good performance ($R \sim 0.1$), the limits of this technique are the increase of weight, the sensitivity to dust and ultraviolet radiation and the increase in the maintenance costs. Alternative roughness distributions are being considered. One example is proposed by Sirovich and Karlsson (1997) who proposed pattern of V-shapes on a surface disposed randomly or aligned with the flow direction, with a drag reduction rate $R \sim 0.15$. A more recent technique is presented by Frohnapfel et al. (2007), the surfaces-embedded grooves. The surface is modified by grooves aligned with the flow direction, which force the fluid near the wall inside the grooves in order to suppress velocity fluctuations in both the normal and tangential directions. Energy dissipation is minimized, then a reduction of drag is observed up to $R = 0.26$. Among passive control techniques compliant coating surfaces, bubbles and polymeric chains are also included.

1.2.2 Open-loop techniques

Open-loop techniques, for which the control law is predetermined, usually operate at large scales. Near-wall flows have been excited by Lorentz forces (Berger et al., 2000; Pang and Choi, 2004), alternating suction and blowing (Segawa et al., 2007), and cross-flow pressure gradients and wall motion (Jung et al., 1992) with the intent to disrupt the self-sustaining turbulence production mechanisms. The forcing has taken the form of spanwise-traveling waves (Du et al., 2002; Itoh et al., 2006), spanwise (Laadhari et al., 1994) or streamwise oscillations (Mito and Kasagi, 1998), and, more recently, of streamwise-traveling waves of spanwise wall velocity (Quadrio et al., 2009).

The choice of addressing open-loop control techniques renders energy effectiveness of the control particularly important. Indeed, the weak side of the open-loop techniques is that they employ forcing at finite amplitudes and thus require a considerable amount of energy when compared to feedback techniques. This energy must be compared to the potential savings to establish the energetic performance of the technique, as done by the performance indicator S (1.3)

1.2.3 Closed-loop techniques

Closed-loop feedback control strategies represent an emerging field of research where the activation is usually applied at the wall as wall-normal distributed transpiration (Bewley et al., 2001; Kim and Bewley, 2007). In a feedback control its input is always determined from sensor signals by a control law, so that it can be more robust and flexible. As reviewed by Kasagi et al. (2009a), the feedback control generally offers better control performance with smaller power consumption than the open-loop control. The

disadvantage is the request of a number of sensors to detect the instantaneous flow state and then control the actuators. These devices are massively located on a wall surface, then, considering that the physical dimensions and response times of these hardware components should be very small, i.e., less than millimeter and millisecond (Kasagi et al., 2009b), fabrication and maintenance of these devices would impose an elevated cost even with rapidly developing of MEMS technology. Thus, the open-control is superior in a sense that it employs a much simpler hardware system than the feedback control, although the better results in term of net energy saved S and gain G.

1.2.4 Spanwise forcing

The important role played by spanwise-forcing techniques among open-loop control schemes has been recently enlighted by Quadrio (2010b). In his work the attention is focused on the attempts carried out in the recent past towards achieving a reduction of the turbulent friction. The choice of the direction in which the wall forcing is applied was somewhat heuristic. At the wall the flow is highly anisotropic, and forcing in each direction brings about its own peculiarities. Forcing along the streamwise direction is usually thought as the less effective means to affect the flow. On intuitive ground, forcing in the wall-normal direction is usually thought of as the "best" way of forcing, but disrupts the natural state of turbulence significantly, at the finite amplitudes typically required by open-loop control. Lastly, forcing in the spanwise direction is found to be quite effective, and this section considers several open-loop techniques based on it: the spanwise-oscillating wall control, the spanwise-traveling waves control and the streamwise-traveling waves.

Spanwise-oscillating wall

The first demonstration of spanwise wall forcing to achieve a significant turbulent drag reduction dates back to almost 20 years ago, with the papers by Jung et al. (1992). They leveraged the idea (Bradshaw and Pontikos, 1985; Coleman et al., 1996) that, in the context of three-dimensional boundary layers, a sudden spanwise pressure gradient generates a transient drop in turbulent friction, eventually followed by a recovery and a realignment of the near-wall flow to the new oblique direction. Making the spanwise pressure gradient harmonic in time, and suitably adjusting its frequency, makes it possible to obtain a sustained reduction of drag. In their original paper, Jung et al. (1992) carried out a numerical DNS study, and assessed the equivalence between an alternating pressure gradient and an harmonic oscillation of the wall, which leads us to the first (and simplest) form of spanwise wall forcing considered in this paper:

$$w = A \sin(\omega t), \tag{1.4}$$

where A is the forcing amplitude, and $T = 2\pi/\omega$ is the forcing period.

The reported performance of the oscillating-wall technique are interesting, with drag reduction rates $R \sim 0.5$ at the low values of Re considered in that early DNS. Experimental confirmation of the drag reduction effect appeared soon thereafter, in particular by Laadhari et al. (1994) for a boundary layer geometry and Choi and Graham (1998) for

a circular pipe. Presently, the challenging aim is the optimization of the oscillating-wall parameters and the understanding of the mechanism of drag reduction.

Spanwise-traveling waves

A spatially non-uniform spanwise forcing was first proposed by Du and Karniadakis (2000) and Du et al. (2002): they simulated via DNS the forcing of the flow with a spanwise-oriented body force as follows:

$$F_z = Ie^{-y/\Delta}\sin(\kappa_z z - \omega t) \tag{1.5}$$

where the forcing, with intensity I and exponentially decreasing away from the wall on a length scale Δ, is modulated in time and in the spanwise direction to form a harmonic wave with wavelength $2\pi/\kappa_z$ that travels along the z direction.

Although non conclusive because of the limited number of parameter combinations, their study is however important since the flow visualizations reported therein clearly point to a significant modification of the near-wall turbulence cycle, with the meandering low-speed streaks almost totally disappearing and a wide, straight ribbon of low-speed fluid appearing in turn. This is contrasted with the flow modifications above the oscillating wall, that does not appear to alter the nature of turbulence regeneration significantly, apart from a periodic left/right tilting of the streaks and the obvious change in Re_τ.

Zhao et al. (2004) translated the spanwise-traveling wave of body force into a space-time distribution of wall acceleration. This is a considerable step forward, since one important parameter exits the picture, making it potentially simpler to determine the general dependence of drag reduction on the wave parameters. If one wants to write the wall velocity forcing equivalent to (1.5) with $\Delta = 0$ in terms of velocity waves, i.e.:

$$w = A\sin(\kappa_z z - \omega t), \tag{1.6}$$

it turns out that a second harmonic component enters the picture. Zhao et al. (2004) indeed found very similar results between wall traveling waves and waves of body force in terms of drag reduction and flow statistics, but with disappointing results in terms of energetics, with negative S for all the parameters tested. However, they too carried out a limited number of simulations, so that the general dependence of flow energetics on the wave parameters is an issue that deserves further consideration.

Streamwise-traveling waves

The spanwise-traveling waves considered by Zhao et al. (2004) are a peculiar type of forcing where the spanwise velocity component is spatially modulated in the spanwise direction to form waves traveling in the spanwise direction. Quadrio et al. (2009) have tried a deceivingly simple modification of the forcing described by Eq. 1.6, namely:

$$w = A\sin(\kappa_x x - \omega t) \tag{1.7}$$

where the forcing still acts along z, but is modulated along x, so that the waves may travel in the streamwise direction with phase speed $c = \omega/\kappa_x$, the sign of which discriminates between forward- and backward-traveling waves.

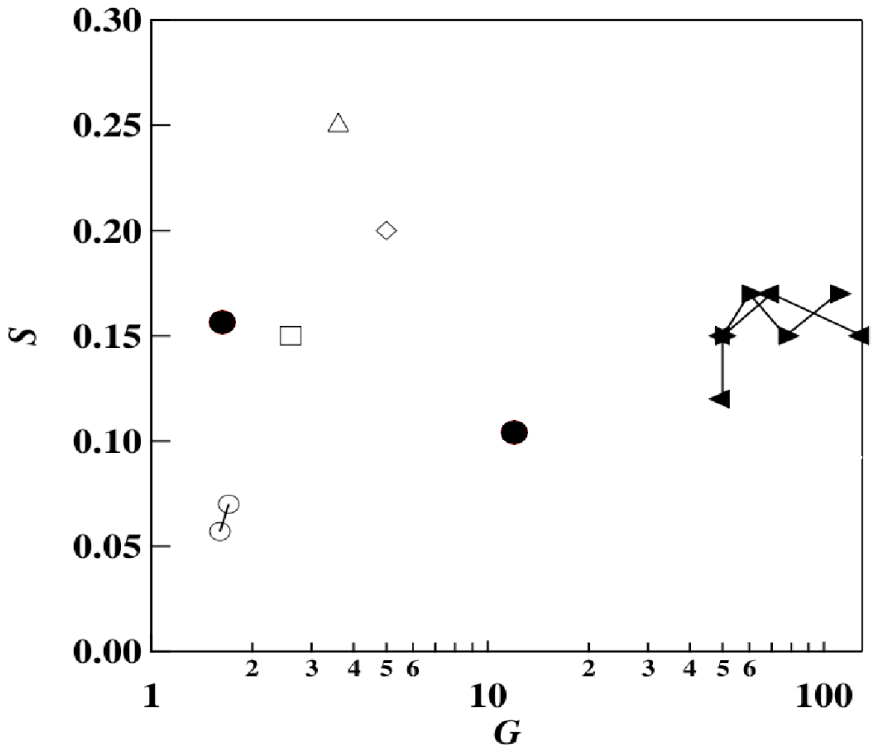

Figure 1.1: Adapted from Kasagi et al. (2009a). Feedback control (black triangles): V-control (right triangles) and sub-optimal control (left triangles) (Iwamoto et al., 2002). Predetermined control (white symbols and black circles): temporally-periodic spanwise wall-oscillation control (white circles) (Quadrio and Ricco, 2004); streamwise traveling wave control (white diamond) (Min et al., 2006); steady streamwise forcing control (white square) (Xu et al., 2007); spatially-periodic spanwise oscillation control (white delta) (Yakeno et al., 2009); streamwise traveling wave control (black circles) (Quadrio et al., 2009)

The waves (1.7) represent a generalization of both the oscillating wall and the stationary waves as limiting cases, for $\kappa_x = 0$ and $\omega = 0$ respectively. Quadrio et al. (2009) carried out a large DNS-based parametric study, exploring several hundredths parameter combination. Although the study was focused on finding best performance in terms of drag reduction at given A, a few calculations have highlighted the extremely good energetic characteristics of the waves (1.7), owing to the notable circumstance that the parameters that yield maximum R are also those that guarantee almost minimal power requested. In the paper a case is documented where $G = 12$ with $S > 0.1$, but it is believed (Quadrio, 2010a) that much better performances are possible. $G = 12$, however, is an high enough gain that a device with an intrinsic efficiency of as low as 8% could still achieve a net saving.

As a summary, figure 1.1 shows a scheme of some flow control techniques as a function of two parameters, the effectiveness of a control algorithm G and the net energy saved rate S, as defined in Kasagi et al. (2009a). It is clearly shown how spanwise-traveling

waves represent the best compromise between efficiency and realization costs, and for this reason this technique seems the most feaseble way to obtain drag reduction.

1.3 Goal of the present work

In the present work, the objective is to gain unique insight into the physics of an incompressible channel flow altered by spanwise wall oscillations. This flow is chosen as it is one of the simplest open-loop drag reduction techniques, with the view that the approach adopted herein will be applied to more complex flows. The focus will be on how the energy transfer is affected by the wall motion and on the role played by the forcing on the modification of the turbulent enstrophy. The numerical results on such balances will be instrumental to determine the behaviour of drag reduction and to extract an analytic formula which allows accurate prediction of drag reduction.

1.4 Flow configuration

An incompressible fully-developed turbulent channel flow between two parallel indefinite flat plates is studied by direct numerical simulations (DNS). The flow is driven by a constant streamwise pressure gradient $P_{,x}$. The coordinates x, y, z define the streamwise, wall-normal and spanwise direction, respectively, and t indicates time. The walls oscillate in phase along the z direction according to

$$U_{zw} = U_{zm} \cos\left(\frac{2\pi t}{T}\right),$$

where U_{zm} is the maximum wall velocity and T is the period of oscillation. Dimensional quantities are indicated by the symbol *. Quantities are scaled by viscous units, i.e. by the kinematic viscosity of the fluid ν^* and the friction velocity $u_\tau^* = \sqrt{\tau_w^*/\rho^*}$, where τ_w^* is the time- and space-averaged wall-shear stress and ρ^* is the density of the fluid. The friction velocity Reynolds number is $Re_\tau = u_\tau^* h^*/\nu^* = 200$, where h^* is half the distance between the channel walls. As $P_{,x}$ is held at a constant value of =-1/Re_τ, the momentum balance at the walls shows that τ_w^* (and therefore Re_τ) is unchanged during the wall motion, which implies that a unique wall-unit scaling is defined. A schematic of the physical domain is shown in figure 1.2.

Details on the DNS code are found in Luchini and Quadrio (2006). Fourier series expansions are used along the homogeneous x and z directions and a fourth-order compact finite-difference discretization scheme is employed along the wall-normal direction. The time advancement is implemented through a combination of an explicit third-order Runge-Kutta scheme for the convection terms and an implicit second-order Crank-Nicolson scheme for the viscous terms. The computational domain has the following dimensions in the x, y, z directions, respectively: $L_x = 6\pi h$, $L_y = 2h$, $L_z = 3\pi h$. The wall-normal direction is discretized by 160 mesh points and 320×320 Fourier modes are used along the homogeneous x and z directions. With the described DNS code a velocity

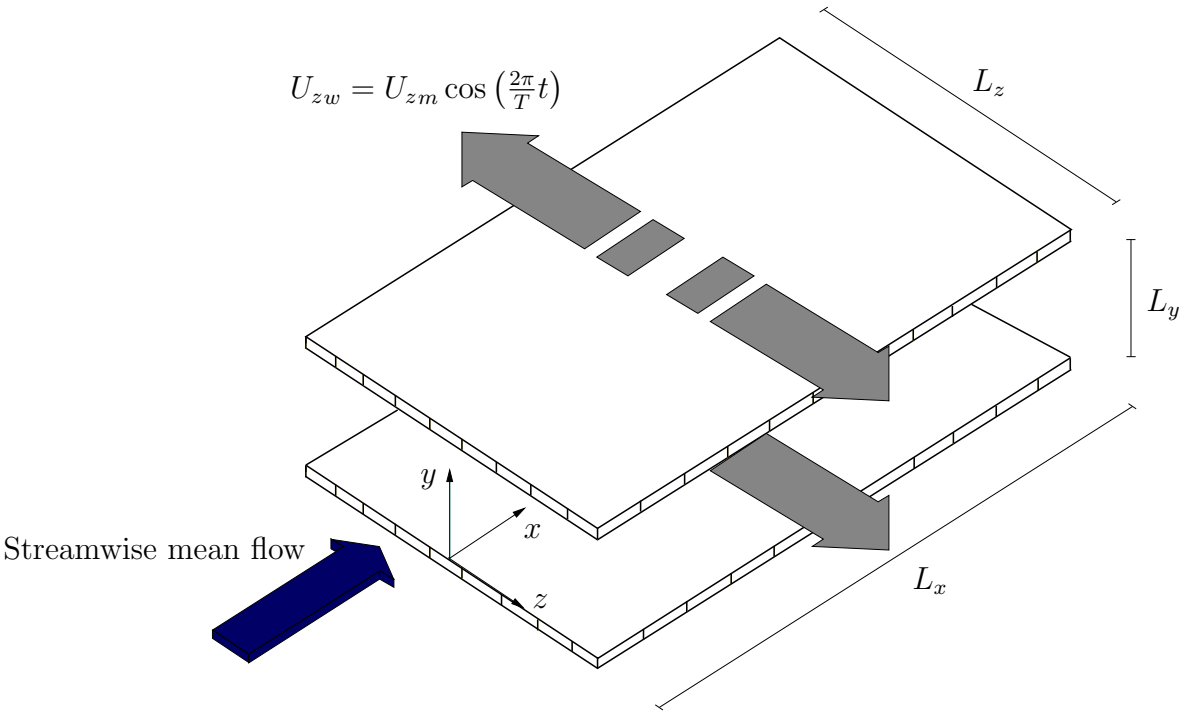

Figure 1.2: Schematic of the physical domain. The lengths L_x, L_y, and L_z are the dimensions of the computational domain along the x, y and z directions, respectively.

field database is calculated for a reference case with fixed walls and for five oscillating-wall cases in which the amplitude of the wall motion is held constant at $U_{zm} = 12$ and the period of oscillation is varied in the range $0 < T \leq 500$. As the simulations are started from a fully-developed turbulent flow field with fixed walls, a temporal transient exists during which the flow adapts to the new oscillating-wall regime (see Quadrio and Ricco (2003) for further details). The numerical procedures to disregard such transient are discussed in Quadrio and Ricco (2004). In that paper the mass flux is kept constant so that the quantity monitored to assess whether the new regime has established is the wall-shear stress, whereas here such quantity is the mass flow rate. We point out that this is the first numerical study on the oscillating-wall problem where the mean pressure gradient is kept constant. After this transient period has been discrted, each flow field has been saved every 0.125 T, i.e. every 0.0625 time units, for 12 periods. Each field of the database has a dimension of 257.1 MB.

The effect of U_{zm} on drag reduction is studied in Quadrio and Ricco (2004).

1.4.1 Flow field decomposition

The velocity and vorticity flow fields are expressed through the Reynolds decomposition, namely as sums of an averaged flow and a fluctuating flow. Once the initial temporal transient has elapsed, quantities can be averaged along the homogeneous x and z directions and in phase as follows

$$\overline{*}(y,t) = \frac{1}{NL_xL_z} \sum_{n=0}^{N-1} \int_0^{L_x} \int_0^{L_z} *(x,y,z,t+nT) \mathrm{d}z \mathrm{d}x,$$

where N is the number of periods of oscillations. Note that averaged quantities henceforth depend on the "window" phase-average time t, $0 \leq t \leq T$.

The velocity and the vorticity fields, $\mathbf{U} = \mathbf{U}(x,y,z,t) = \{U_x, U_y, U_z\}$ and $\mathbf{\Omega} = \mathbf{\Omega}(x,y,z,t) = \{\Omega_x, \Omega_y, \Omega_z\}$, are decomposed as follows

$$\mathbf{U} = \{\overline{U_x}(y,t), 0, \overline{U_z}(y,t)\} + \{u_x, u_y, u_z\}, \quad \mathbf{\Omega} = \{\overline{\Omega_x}(y,t), 0, \overline{\Omega_z}(y,t)\} + \{\omega_x, \omega_y, \omega_z\},$$

where $\overline{\Omega_x} = \overline{U_{z,y}}$ and $\overline{\Omega_z} = -\overline{U_{x,y}}$ in our case of spanwise wall oscillations. We also define the x-, $z-$, phase-averaged vorticity squared, i.e. the enstrophy, as follows:

$$\overline{\mathbf{\Omega} \cdot \mathbf{\Omega}} = \overline{\Omega_i}\,\overline{\Omega_i} + \overline{\omega_i \omega_i}.$$

The Einstein summation convention of repeated indexes is adopted henceforth. The time average is defined as

$$\langle * \rangle (y) = \frac{1}{T} \int_0^T *(y,t) \mathrm{d}t,$$

where $*(y,t)$ here refers to a quantity or a product of two quantities averaged along x, z and in phase. All the statistical samples are doubled by averaging quantities on both halves of the channel. A quantity is defined as *global* when it is averaged along x,z, in phase (or it is a product of two such quantities), on both halves of the channel, in time and integrated along y from the wall at $y = 0$ to the centerline of the channel at $y = h$. A transport equation is defined as global when its terms are global.

1.4.2 Definition of turbulent drag reduction

The skin-friction coefficient is defined as $C_f = 2\tau_w^*/\rho^* U_b^{*2}$, where U_b^* is the bulk velocity

$$U_b^* = \frac{1}{h^*}\int_0^{h^*} \langle \overline{U_x^*} \rangle \, \mathrm{d}y^*. \tag{1.8}$$

The turbulent drag reduction rate, R, is calculated from the variation of C_f with respect to the fixed-wall value

$$R = \frac{C_{f,r} - C_{f,o}}{C_{f,r}},$$

where the subscripts r and o indicate the fixed-wall and oscillating-wall cases, respectively. In the present case of constant $P_{,x}$, the R is due to the increase of mass flow rate. As

$$C_f = \frac{2}{U_b^2}, \tag{1.9}$$

the R may be written as

$$R = \frac{U_{b,o}^2 - U_{b,r}^2}{U_{b,o}^2}. \tag{1.10}$$

Note that the percent change in skin-friction coefficient R does not coincide with the percent change in mean streamwise kinetic energy because the squared bulk velocity in the oscillating-wall case is at the denominator in (1.10), while the variation of kinetic energy is expressed with respect to the squared bulk velocity in the fixed-wall case.

1.5 Turbulence statistics

The effect of the wall oscillation on $\langle \overline{U_x} \rangle$ is shown in figure 1.3 ($T = 100$, R=0.31). The velocity $\langle \overline{U_x} \rangle$ increases significantly throughout the channel while the mean wall-shear stress remains constant. Figure 1.4 displays the R dependence on T. The drag reduction increases sharply up to the optimum $T_{opt} \approx 70$ and then decays at a slower rate. This behaviour has been well documented by previous numerical studies (see Quadrio and Ricco (2004) for further details). The optimum period at fixed maximum wall velocity has been usually reported as $T \approx 100 - 125$ in previous studies conducted at constant mass flow rate, where u_τ^* for the fixed wall case was employed for scaling. The root-mean-square (rms) of the turbulent velocity fluctuations, defined as $b_{rms} = \left\langle \overline{b^2} \right\rangle^{1/2}$, where b represents u_x, u_y or u_z, and the Reynolds stresses $\langle \overline{u_x u_y} \rangle$ are shown in figure 1.5 (left). The wall motion primarily affects $u_{x_{rms}}$ up to $y \approx 30$; the peak decreases by about 15% and it shifts from $y \approx 14$ to $y \approx 20$. The profile of $u_{y_{rms}}$ is largely unvaried, while $u_{z_{rms}}$ increases up to $y \approx 40$. The Reynolds stresses $\langle \overline{u_x u_y} \rangle$ are attenuated up to $y \approx 60$. The wall oscillation induces the additional Reynolds stresses $\overline{u_y u_z}$, shown in figure 1.5 (right). This term is null in the fixed-wall case. Its maximum is located at $y \approx 16$, almost at the same position of the $u_{x_{rms}}$ maximum. At opposite phases of the cycle, the $\overline{u_y u_z}$ profiles show the same trend with opposite sign, which leads to $\langle \overline{u_y u_z} \rangle = 0$.

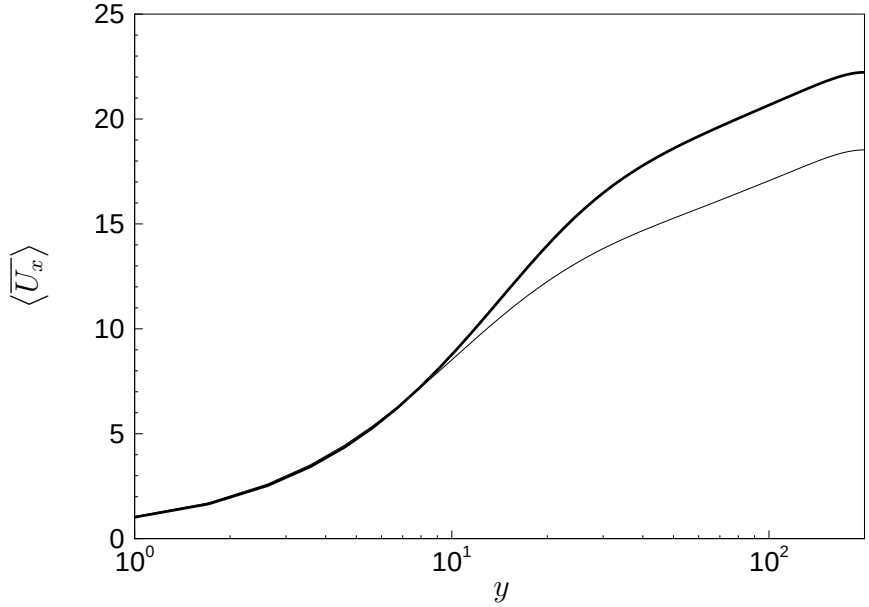

Figure 1.3: Wall-normal profiles of $\langle \overline{U_x} \rangle$ for fixed-wall (thin line) and oscillating-wall (thick line) conditions at $T = 100$.

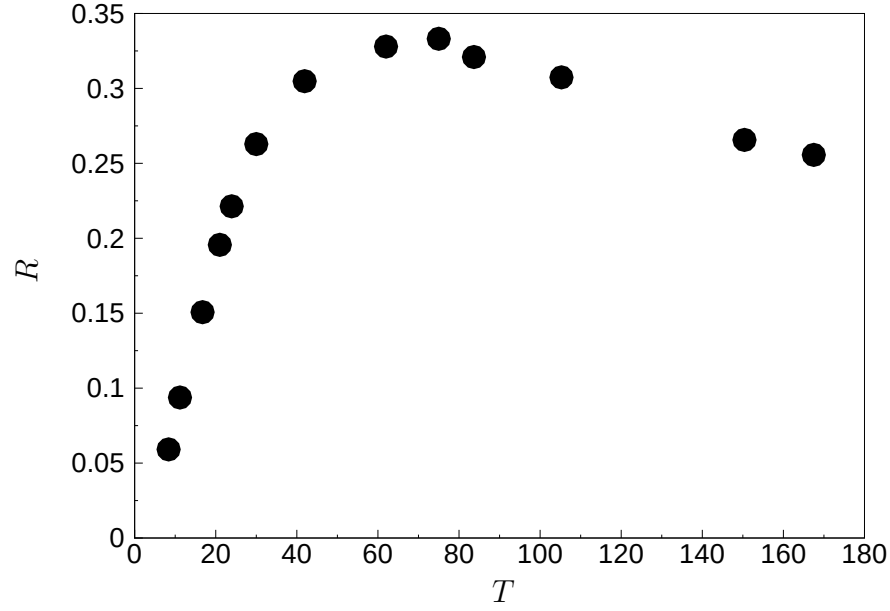

Figure 1.4: Drag reduction rate R obtained with the oscillating wall as a function of the oscillating period T.

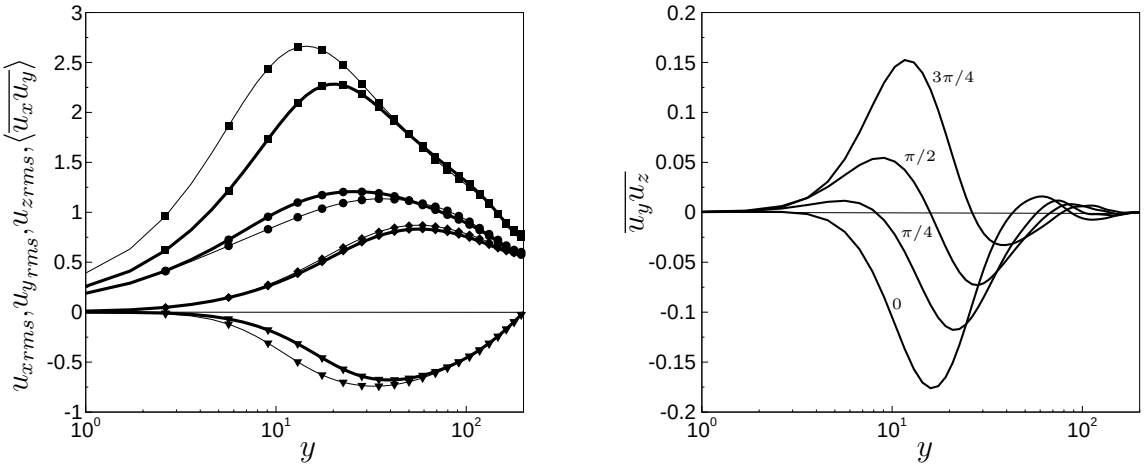

Figure 1.5: Left: Wall-normal profiles of rms of velocity fluctuations and of Reynolds stresses $\langle \overline{u_x u_y} \rangle$ for fixed-wall (thin lines) and oscillating-wall (thick lines - $T = 100$) cases. Squares: u_{xrms}, diamonds: $u_{y_{rms}}$, circles: u_{zrms}, triangles: $\langle \overline{u_x u_y} \rangle$. Right: Wall-normal profiles of Reynolds stresses $\overline{u_y u_z}$ at different phases of the cycle for $T = 100$.

Chapter 2

Energy balance

The DNS database is analyzed through the statistics of the balance equations of kinetic energy for the mean and fluctuating flow, and the global balance of energy.

2.1 Balance of energy

Relation (1.9) shows the importance of investigating the increment of U_b to understand the mechanism of C_f reduction. As a first step, we therefore study the transport equations for the mean kinetic energy (MKE), $\left(\overline{U_x}^2 + \overline{U_z}^2\right)/2$, where U_b appears explicitly, and for the turbulent kinetic energy (TKE), $\overline{q^2}/2$, where $q^2 = u_i u_i$. These two equations are summed to obtain the global balance for the total kinetic energy.

2.1.1 Balance equation for the mean kinetic energy

The time-dependent transport equation for MKE reads

$$\begin{aligned}\underbrace{\left(\overline{U_x}^2 + \overline{U_z}^2\right)_{,t}/2}_{1} + \underbrace{\overline{U_x}P_{,x}}_{2} = \underbrace{\overline{u_x u_y}\,\overline{U_x}_{,y}}_{3} + \underbrace{\overline{u_y u_z}\,\overline{U_z}_{,y}}_{4} - \underbrace{\left(\overline{u_x u_y}\,\overline{U_x}\right)_{,y}}_{5} - \underbrace{\left(\overline{u_y u_z}\,\overline{U_z}\right)_{,y}}_{6} \\ + \underbrace{\left(\overline{U_x}\;\overline{U_x}_{,y}\right)_{,y}}_{7} + \underbrace{\left(\overline{U_z}\;\overline{U_z}_{,y}\right)_{,y}}_{8} - \underbrace{\left(\overline{U_x}_{,y}\right)^2}_{9} - \underbrace{\left(\overline{U_z}_{,y}\right)^2}_{10}.\end{aligned} \tag{2.1}$$

Term 1 denotes the temporal change of MKE and term 2 is the work done by $P_{,x}$, i.e. the energy used to drive the flow along x. Thanks to the wall oscillation, the system absorbs more kinetic energy than in the fixed-wall case through the increment of $\overline{U_x}$. Term 3 is the work of deformation carried out by the Reynolds stresses $\overline{u_x u_y}$ and it exchanges energy between the mean flow and the fluctuating flow. Term 4 indicates the work of deformation done by the Reynolds stresses $\overline{u_y u_z}$. Similarly to term 3, it transfers energy between the mean flow and the fluctuating flow. Terms 3 and 4 appear with the opposite sign in the TKE equation, as shown in §2.1.2. The transport works performed by the Reynolds stresses $\overline{u_x u_y}$ and $\overline{u_y u_z}$ are denoted by terms 5 and 6, respectively. Terms 7 and 8 are the transport works done by the mean streamwise and spanwise viscous stresses,

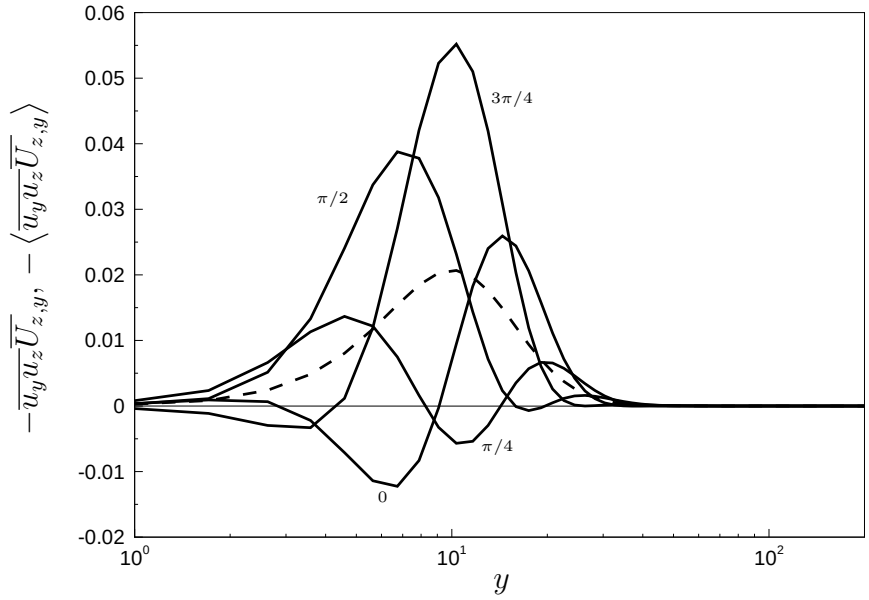

Figure 2.1: Wall-normal profiles of $-\overline{u_y u_z}\overline{U}_{z,y}$ at different phases (solid lines) and $-\left\langle \overline{u_y u_z}\overline{U}_{z,y} \right\rangle$ (dashed line) for $T = 100$.

respectively. Term 9 is the viscous dissipation of MKE by the mean streamwise flow gradient, while term 10 is the viscous dissipation by the mean spanwise flow gradient.

The second term in 1 and terms 4, 6, 8, 10 are directly related to the wall oscillation because $\overline{U}_z$ appears explicitly in their expressions. The turbulent production term 4, $-\overline{u_y u_z}\overline{U}_{z,y}$, which is absent in the fixed-wall case because $\overline{u_y u_z}$ and $\overline{U}_z$ are null, is shown in figure 2.1 at different phases of the cycle for $T = 100$. Although it is negative during part of the cycle (mainly for $y < 15$, when it instantaneously extracts energy from the turbulent fluctuations to enhance MKE), it is positive for most of the cycle, i.e. its average contribution is to transfer MKE to the turbulent fluctuations (see dashed line in figure 2.1).

As the interest resides in the change of U_b, which is a global quantity as defined in (1.8), the MKE equation (2.1) is now averaged in time and integrated along y in order to make U_b appear in the energy balance. Time averaging eliminates term 1 because of time periodicity. Terms 2, 3, 4, 9, 10 are retained and so is term 8 because $\overline{U}_z$ is non zero at $y = 0$. Terms 5 and 6 disappear when made global because $\overline{u_x u_y}$ and $\overline{u_y u_z}$ are null at $y = 0$ and at $y = h$. Term 7 becomes null because $\overline{U}_x$ is null at $y = 0$ and $\overline{U}_{x,y}$ is so at $y = h$.

The global transport equation for MKE is

$$U_b + \underbrace{\left\langle U_{zw}\, U_{z,y}\big|_{y=0}\right\rangle}_{\mathcal{S}_w} = \underbrace{-\int_0^h \left\langle \overline{u_x u_y}\,\overline{U_x}_{,y}\right\rangle \mathrm{d}y}_{\mathcal{P}_{u_x u_y}} \underbrace{-\int_0^h \left\langle \overline{u_y u_z}\,\overline{U_z}_{,y}\right\rangle \mathrm{d}y}_{\mathcal{P}_{u_y u_z}} + \underbrace{\int_0^h \left\langle \left(\overline{U_x}_{,y}\right)^2\right\rangle \mathrm{d}y}_{\mathcal{D}_{U_x}} + \underbrace{\int_0^h \left\langle \left(\overline{U_z}_{,y}\right)^2\right\rangle \mathrm{d}y}_{\mathcal{D}_{U_z}} \tag{2.2}$$

The bulk velocity U_b comes from term 2 in (2.1) and represents the global energy pumped into the system through $P_{,x}$. Term $\mathcal{S}_w$ denotes the power spent to move the walls against the frictional resistance of the fluid, and it stems from the transport term 8 in (2.1). It is the energy input given by the wall motion. Terms $\mathcal{P}_{u_x u_y}$ and $\mathcal{P}_{u_y u_z}$ indicate the global TKE production terms related to $\overline{u_x u_y}$ and $\overline{u_y u_z}$, respectively, and originate from terms 3 and 4 in (2.1). The global viscous dissipation terms due to the gradients of the mean streamwise and spanwise velocity components are denoted by $\mathcal{D}_{U_x}$ and $\mathcal{D}_{U_z}$, and come from terms 9 and 10 in (2.1), respectively. Equation (2.2) represents the first step toward understanding drag reduction because U_b now appears explicitly. It states that part of the energy inputs, U_b and $\mathcal{S}_w$, is transferred to the turbulence via $\mathcal{P}_{u_x u_y}$ and $\mathcal{P}_{u_y u_z}$ and part is dissipated into heat through $\mathcal{D}_{U_x}$ and $\mathcal{D}_{U_z}$.

2.1.2 Balance equation for the turbulent kinetic energy

The time-dependent transport equation for TKE is studied in this section. It reads

$$\underbrace{\overline{q^2}_{,t}/2}_{1} = \underbrace{-\left[\overline{u_y\left(p+q^2/2\right)}\right]_{,y}}_{2} \underbrace{-\overline{u_x u_y}\,\overline{U_x}_{,y}}_{3} \underbrace{-\overline{u_y u_z}\,\overline{U_z}_{,y}}_{4} \underbrace{+\overline{q^2}_{,yy}/2}_{5} \underbrace{-\overline{u_{i,j}u_{i,j}}}_{6} \tag{2.3}$$

where p is the turbulent pressure. The temporal change of TKE is denoted by term 1, while term 2 represents the work of transport done by the total dynamic pressure of turbulence. Terms 3 and 4 indicate the works of deformation done by Reynolds stresses $\overline{u_x u_y}$ and $\overline{u_y u_z}$ by which energy is exchanged between the mean flow and the fluctuating flow. These terms appear in the MKE equation (2.1) with opposite sign. Terms 5 and 6 together represent the combined effect of the work done by the viscous shear stresses of the turbulent motion and of the viscous dissipation of TKE into heat. Term 6 is often referred to as the pseudo-dissipation (see Pope (2000) at page 132). The turbulent production term 4, $\overline{u_y u_z}\,\overline{U_z}_{,y}$, is the only one containing $\overline{U_z}$ explicitly.

Analogously to the analysis of the MKE equation, time averaging and integration along y lead to the following simplifications. Term 1 disappears because of time periodicity. Term 2 becomes null upon y-integration because of the no-slip condition at $y = 0$ and $\overline{u_y p} = \overline{u_y q^2/2} = 0$ at $y = h$. Term 5 is also null because

$$\int_0^h \left\langle \overline{q^2}_{,yy}\right\rangle \mathrm{d}y = \int_0^h \left\langle \overline{q^2}_{,y}\right\rangle_{,y} \mathrm{d}y = \left\langle \overline{q^2}_{,y}\right\rangle\Big|_{y=h} - \langle \overline{qq}_{,y}\rangle\big|_{y=0} = 0,$$

as $\overline{q^2}_{,y} = 0$ at $y = h$ and $q = 0$ at $y = 0$.

The global transport equation for TKE is

$$\underbrace{-\int_0^h \left\langle \overline{u_x u_y}\,\overline{U_x}_{,y} \right\rangle \mathrm{d}y}_{\mathcal{P}_{u_x u_y}} \underbrace{-\int_0^h \left\langle \overline{u_y u_z}\,\overline{U_z}_{,y} \right\rangle \mathrm{d}y}_{\mathcal{P}_{u_y u_z}} - \int_0^h \left\langle \overline{u_{i,j} u_{i,j}} \right\rangle \mathrm{d}y = 0 \tag{2.4}$$

where $\mathcal{P}_{u_x u_y}$ and $\mathcal{P}_{u_y u_z}$ are as in (2.2). The next-to-last equation at page 74 in Hinze (1975) shows that the last term in (2.4) is the global TKE dissipation,

$$\mathcal{D}_T \equiv \int_0^h \left\langle \overline{u_{i,j}\left(u_{i,j} + u_{j,i}\right)} \right\rangle \mathrm{d}y = \int_0^h \left\langle \overline{u_{i,j} u_{i,j}} \right\rangle \mathrm{d}y \tag{2.5}$$

Equation (2.4) may therefore be written as

$$-\mathcal{P}_{u_x u_y} - \mathcal{P}_{u_y u_z} = \mathcal{D}_T. \tag{2.6}$$

The balance in (2.6) indicates that the global TKE produced through the mean flow gradients, $\mathcal{P}_{u_x u_y}$ and $\mathcal{P}_{u_y u_z}$, is dissipated into heat by the viscous stresses of the turbulence. The global dissipation $\mathcal{D}_T$ increases by about 18% when the walls are in motion for $T = 100$. The production $\mathcal{P}_{u_x u_y}$ contributes to about 73% of this change and $\mathcal{P}_{u_y u_z}$ to about 27%. Figure 2.2 shows the wall-normal profiles of the three terms whose integrals compose the balance (2.6). The time average of term 4 in (2.3), $\left\langle \overline{u_y u_z}\,\overline{U_z}_{,y} \right\rangle$, is much smaller than term 3, $\left\langle \overline{u_x u_y}\,\overline{U_x}_{,y} \right\rangle$, which is the only production term in the fixed-wall case.

By use of the fluctuating vorticity, term 6 in (2.3) becomes (Pope, 2000)

$$\overline{u_{i,j} u_{i,j}} = \overline{\omega_i \omega_i} + \overline{u_i u_j}_{,ij} \tag{2.7}$$

The global dissipation of TKE in (2.3) becomes

$$\mathcal{D}_T = \int_0^h \left\langle \overline{\omega_i \omega_i} \right\rangle \mathrm{d}y, \tag{2.8}$$

which follows from the substitution of (2.7) into (2.5), from the periodicity along the homogeneous x and z directions, from the velocity fluctuations being zero at $y = 0$ and from $\overline{v v}_{,y} = 0$ at $y = h$. Note that the viscous dissipation of the total mechanical energy, i.e. $\mathcal{D}_M + \mathcal{D}_T$, is equal to the global enstrophy only in the case of stationary boundaries (Davidson, 2004), and therefore not in the oscillating-wall case. However, equation (2.8) is valid for the wall-oscillation case because the turbulent fluctuations vanish at the walls.

2.1.3 Total kinetic energy balance

In the previous section, the global transport equations for MKE, (2.2), and TKE, (2.4), have been studied. By summing these two equations, the global balance for the total mechanical energy is found

$$U_b + \mathcal{S}_w = \mathcal{D}_{U_x} + \mathcal{D}_{U_z} + \mathcal{D}_T. \tag{2.9}$$

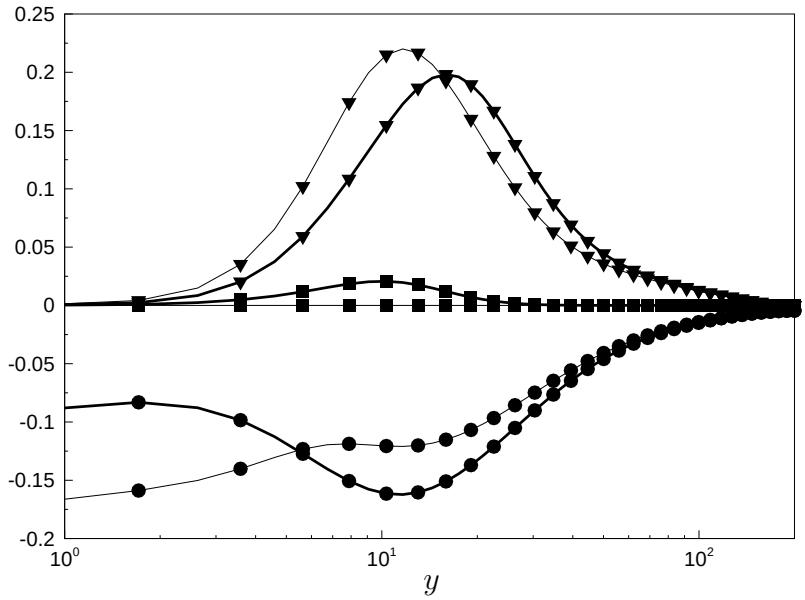

Figure 2.2: Wall-normal profiles of production terms $-\left\langle \overline{u_x u_y} \overline{U}_{x,y} \right\rangle$ (term 3 in (2.3), denoted by triangles), $-\left\langle \overline{u_y u_z} \overline{U}_{z,y} \right\rangle$ (term 4 in (2.3), squares), and of pseudo-dissipation $-\left\langle \overline{(u_{i,j})^2} \right\rangle$ (term 6 in (2.3), circles) for fixed-wall (thin lines) and oscillating-wall cases for $T = 100$ (thick lines). Integration of these terms along y gives $\mathcal{P}_{u_x u_y}$, $\mathcal{P}_{u_y u_z}$ and $\mathcal{D}_T$, respectively, which compose the global TKE transport equation (2.6).

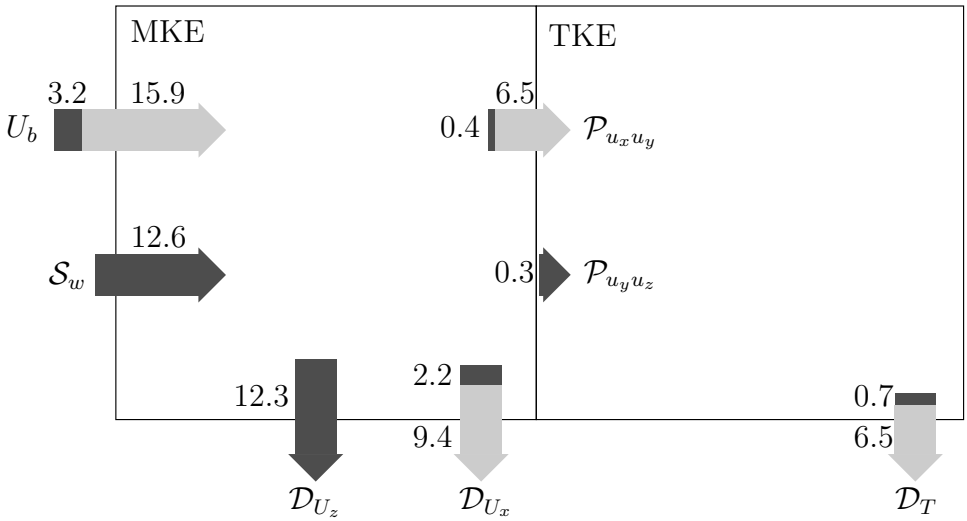

Figure 2.3: Schematic of the global energy balance for the total mechanical energy for $T = 100$. The numbers indicate the magnitude of the terms and their change during the wall oscillation. The light grey portions of arrows denote the contributions at fixed-wall conditions, while the dark grey arrows or portions of arrows indicate the changes due to the wall motion.

The energy input U_b to drive the flow along the streamwise direction, given by $P_{,x}$, and the power $\mathcal{S}_w$, spent to enforce the wall motion, are dissipated into heat through the viscous action of the mean streamwise and spanwise flow gradients, denoted by $\mathcal{D}_{U_x}$ and $\mathcal{D}_{U_z}$ respectively, and through the viscous dissipation $\mathcal{D}_T$ of the turbulent fluctuations. Note that, as shown by Laadhari (2007), $\mathcal{D}_T \gg \mathcal{D}_{U_x}$ as $Re_\tau \to \infty$, so that (2.9) simplifies in this limit as $\mathcal{D}_{U_x}$ may be neglected.

Figure 2.3 summarizes the global energy balance for $T = 100$. The two boxes represent MKE and TKE; the light grey portions of arrows indicate the energy terms in the fixed-wall configuration, while the dark grey arrows or portions of arrows denote the energy transfers due to the wall motion. The schematic distinctly shows that the production terms, $\mathcal{P}_{u_x u_y}$ and $\mathcal{P}_{u_y u_z}$, only transfer energy "internally" between MKE and TKE, therefore disappearing from the total energy balance (2.9).

As discussed in §1.5, as C_f and U_b are related, the aim is to study how the wall motion acts on U_b to discern information on R. The total energy balance (2.9) is therefore analyzed in more detail because it contains U_b explicitly. The two terms containing $\overline{U_z}$, i.e. $\mathcal{S}_w = 12.6$ and $\mathcal{D}_{U_z} = 12.3$, almost balance each other; the difference is about 1% and it is due to $\mathcal{P}_{u_y u_z}$, which is absent in (2.9) and much smaller than the other terms in (2.9). It is therefore sufficient to investigate how the wall oscillation affects the dynamics of the two remaining relevant terms, i.e. $\mathcal{D}_{U_x}$ and $\mathcal{D}_T$, to gain insight on the changes of U_b.

In order to discern how the wall motion acts on $\mathcal{D}_{U_x}$, the transport equation for $\left(\overline{U_x}_{,y}\right)^2$, the integrand of $\mathcal{D}_{U_x}$ (see (2.2)), is studied. It reads

$$\frac{1}{2}\left[\left(\overline{U_x}_{,y}\right)^2\right]_{,t} = -\overline{u_x u_y}_{,yy}\overline{U_x}_{,y} + \frac{1}{2}\left[\left(\overline{U_x}_{,y}\right)^2\right]_{,yy} - \overline{U_x}_{,yy} \tag{2.10}$$

The spanwise velocity $\overline{U_z}$ is absent in the transport equation for $\left(\overline{U_x}_{,y}\right)^2$, which implies that the oscillating wall does not influence the dynamics of the mean streamwise flow directly. The focus is then directed toward understanding how the wall motion affects the dynamics of the global dissipation $\mathcal{D}_T$ (or the global fluctuating enstrophy, see (2.8)), given by the viscous action of the turbulent fluctuations.

Chapter 3

Enstrophy balance

Following the previous chapter analysis, the statistics for the fluctuating enstrophy balance equation are calculated from the DNS database in order to explain the drag reduction behaviour due to spanwise forcing.

3.1 Enstrophy instead of dissipation

Through the global balance of the total energy, it has been shown that, in order to understand how the wall motion affects C_f, the variation of the turbulent energy dissipation $\mathcal{D}_T$ must be studied. As shown in (2.8), $\mathcal{D}_T$ can be expressed as the global turbulent enstrophy. In section 3.2.3 it is demonstrated by an order-of-magnitude analysis, that studying transport equation for turbulent dissipation is in reality the same as studying that for the turbulent enstrophy. As the main purpose is to evince one or some terms directly responsible for drag reduction, the two different approaches lead to the same result. The choice of studying the enstrophy balance is suggested by the number of literature and research works about enstrophy and vorticity related to flow control instead of that about turbulent dissipation. Besides the fact that the expression for $\mathcal{D}_T$ in terms of the turbulent enstrophy is more compact than if the turbulent dissipation is used (compare (2.8) with (2.5)), the transport equation for the turbulent enstrophy has the main advantage over the dissipation equation that the turbulent pressure does not need to be computed. (This advantage is shared by the Orr-Sommerfeld and vorticity formulations of the Navier-Stokes equations over the framework involving primitive variables.) Furthermore, the physical meaning conveyed by the enstrophy equation is arguably more immediate than the one provided by the dissipation equation; for example, terms 2 and 3 in (3.1) denote production of vorticity, while the corresponding terms in the dissipation equation indicate production of turbulent dissipation.

3.2 Balance of enstrophy

The transport equation for the fluctuating component of enstrophy is therefore investigated in this section. It reads (Tennekes and Lumley, 1972)

$$\begin{aligned}\underbrace{\overline{\omega_i\omega_i}_{,t}/2}_{1} = &\underbrace{\overline{\omega_x\omega_y}\,\overline{U}_{x,y}}_{2} + \underbrace{\overline{\omega_z\omega_y}\,\overline{U}_{z,y}}_{3} + \underbrace{\overline{\omega_j u_{x,j}}\,\overline{U}_{z,y}}_{4} - \underbrace{\overline{\omega_j u_{z,j}}\,\overline{U}_{x,y}}_{5} - \underbrace{\overline{u_y\omega_x}\,\overline{U}_{z,yy}}_{6} + \\ &\underbrace{\overline{u_y\omega_z}\,\overline{U}_{x,yy}}_{7} + \underbrace{\overline{\omega_i\omega_j u_{i,j}}}_{8} - \underbrace{\overline{u_y\omega_i\omega_i}_{,y}/2}_{9} + \underbrace{\overline{\omega_i\omega_i}_{,yy}/2}_{10} - \underbrace{\overline{\omega_{i,j}\omega_{i,j}}}_{11}.\end{aligned} \tag{3.1}$$

The physical meaning of each term is as follows. Term 1 indicates the time rate of change of the turbulent enstrophy due to the wall motion. Terms 2 and 3 are the production (or removal) of turbulent vorticity caused by stretching (or squeezing) of vorticity fluctuations by the mean flow gradients $\overline{U}_{x,y}$ and $\overline{U}_{z,y}$, respectively. Terms 4 and 5 indicate the production of mean and turbulent enstrophy by the stretching of fluctuating vorticity through the fluctuating strain rates $u_{x,j}$ and $u_{z,j}$, respectively. These terms occur in the equation for the mean enstrophy with the same sign. Terms 6 and 7 represent the exchange of fluctuating vorticity between the mean enstrophy and the turbulent enstrophy due to the gradients of streamwise and spanwise mean vorticity, respectively. They are analogous to the turbulent kinetic energy production terms in the MKE and TKE equations. Term 8 is the production of turbulent enstrophy by stretching of turbulent vorticity through turbulent velocity gradients. Term 9 denotes the transport of turbulent enstrophy by the fluctuating wall-normal velocity component. Term 10 is the viscous transport of turbulent enstrophy and term 11 is the viscous dissipation of turbulent enstrophy. The only terms in (3.1) that become null when the equation is made global are term 1 when averaged in time because of time periodicity and term 9 when integrated along y.

Differently from the case of the transport equation (2.10) for $(\overline{U}_{x,y})^2$, which contributes to $\mathcal{D}_{U_x}$ (see (2.2)), the velocity $\overline{U}_z$ appears explicitly in terms 3, 4 and 6 of the turbulent enstrophy equation (3.1). These terms arise only when the wall oscillates. This indicates that the action of the spanwise motion is direct on the turbulent enstrophy, and therefore on the global turbulent dissipation $\mathcal{D}_T$. As this quantity increases during the wall motion, it is worth studying how these oscillating-wall terms contribute to modify the enstrophy balance, thereby affecting $\mathcal{D}_T$, and, in turn, U_b through (2.9) and C_f through (1.9).

Figure 3.1 shows the profiles of the time-averaged terms in the turbulent enstrophy balance (3.1) for fixed-wall (top) and oscillating-wall conditions for $T = 100$ (bottom). The numbers refer to the terms in (3.1) and the thick lines represent the terms only occuring when the walls are in motion. The fixed-wall profiles compare successfully with the ones in Antonia and Kim (1994), Gorski et al. (1994) and Abe et al. (2009). (Note that in Gorski et al. (1994) and Abe et al. (2009) the terms are multiplied by a factor of 2.) In the oscillating-wall case, the vorticity production term 3, $\langle\overline{\omega_z\omega_y}\,\overline{U}_{z,y}\rangle$, is dominant in the proximity of the wall, $y < 10$, over terms 4 and 6, and over the production and transport terms already present in the fixed-wall case, i.e. terms 2,5,7,8,10. Term 3 peaks at $y \approx 6$ and distinctly affects term 11, the time-averaged dissipation of turbulent enstrophy, at the edge of the viscous sublayer and in the lower part of the buffer region,

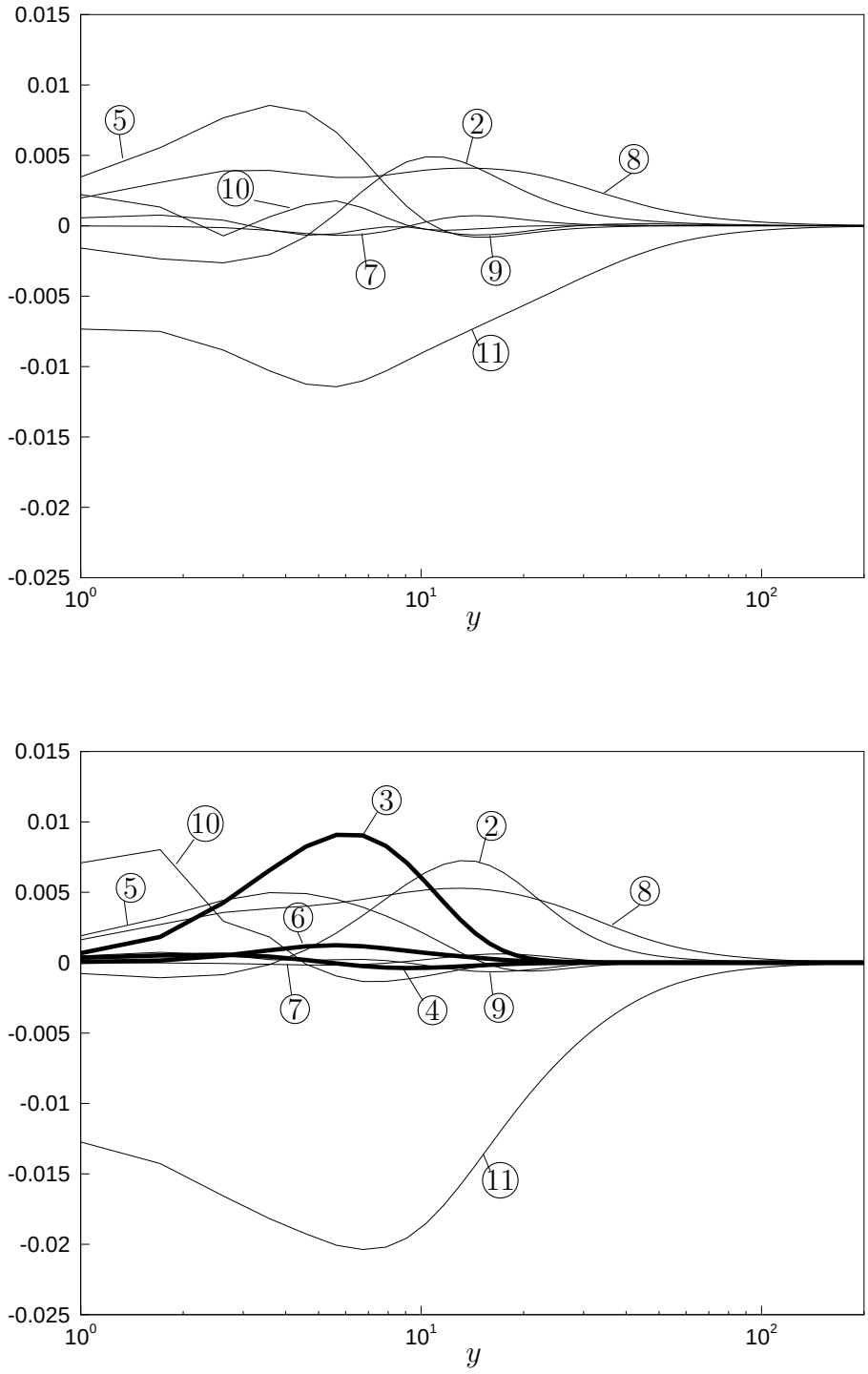

Figure 3.1: Wall-normal profiles of terms in transport equation (3.1) for turbulent enstrophy in the fixed-wall case (top) and the oscillating-wall case (bottom) for $T = 100$.

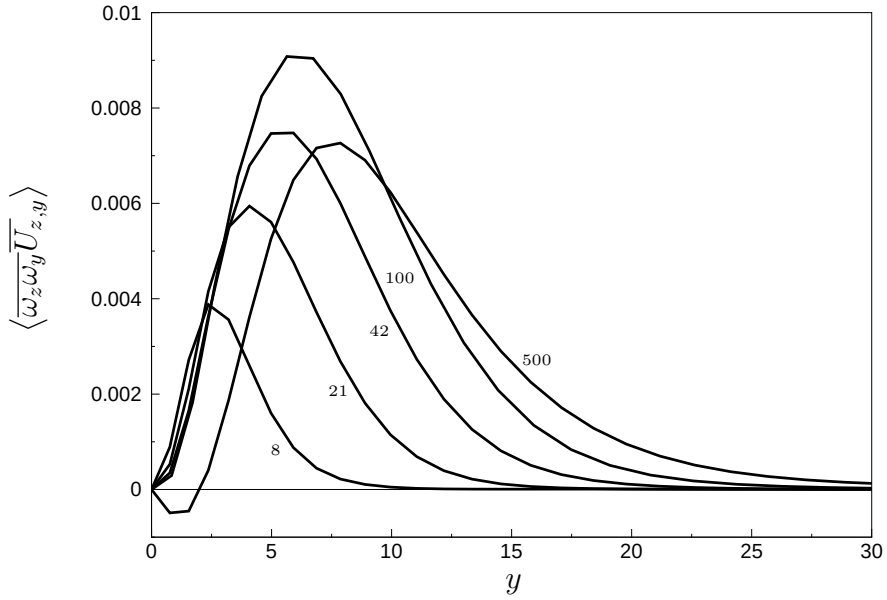

Figure 3.2: Wall-normal profiles of $\left\langle \overline{\omega_z \omega_y} \overline{U}_{z,y} \right\rangle$ at different T.

as clear from the similar shapes of the profiles for $2 < y < 20$. Figure 3.2 shows that the vorticity production term 3 increases with T up to periods larger than the optimum T for drag reduction. In a very thin near-wall layer, $y < 2$, term 3 is small. Term 10, the viscous transport of turbulent enstrophy, is instead responsible for the intense increase of dissipation of turbulent enstrophy there. While the production term $\left\langle \overline{\omega_z \omega_y} \overline{U}_{z,y} \right\rangle$ highlights the direct action of the spanwise shear layer on the turbulent enstrophy, the increase of the production term 2, $\left\langle \overline{\omega_x \omega_y} \overline{U}_{x,y} \right\rangle$, outlines the indirect effect of the wall motion caused by the increment of $\overline{U}_{x,y}$. Term 3 is primarily dominant near the wall, whereas term 2 increases at higher locations. This is because term 3 is dictated by the near-wall spanwise velocity $\overline{U}_z$, while $\overline{U}_{x,y}$ only varies significantly for $y > 15$ being the wall-shear stress constant (see figure 1.4). We finally note that the production term 5, $\left\langle \overline{\omega_j u_{z,j}} \overline{U}_{x,y} \right\rangle$, decreases substantially in the oscillating-wall case, while the production and transport terms 8 and 9, which only involve fluctuating quantities, are largely unaffected.

3.2.1 Order-of-magnitude analysis

The order of magnitude of the terms in (3.1) arising because of the wall motion can be estimated through an analysis similar to the one carried out for example by Tennekes and Lumley (1972) at pages 89 and 90. Two symbols are adopted, following the introductory discussion on the use of symbols in Tennekes and Lumley (1972). The symbol $\sim$ denotes a crude approximation; it highlights the dependence of the term under scrutiny on the characteristic length and velocity scales of the turbulent motion. Upon decomposing an enstrophic term into sub-terms containing the fluctuating velocity components, the

symbol $\mathcal{O}$ denotes its magnitude in terms of the dominant sub-term. In Tennekes and Lumley (1972), a generic length scale is assumed to describe the mean flow motion and the Taylor microscale is taken as the reference length scale for the turbulent fluctuations in all directions, suggesting that such an analysis is useful primarily for isotropic turbulence. However, our interest is on the wall-bounded turbulence dynamics with oscillations, which is strongly anisotropic. It is therefore necessary to distinguish different length and velocity scales along the three Cartesian directions. Although the following analysis may appear approximate, the estimates of the orders of magnitude match the numerical calculations well.

The near-wall turbulent dynamics is characterized by three distinct length scales. The length scale of the disturbance along the z direction can be taken as $\lambda_z = \mathcal{O}(100)$, namely the characteristic spacing of the low-speed streaky structures (Kline et al., 1967). As shown by Ricco (2004), the streaks spacing increases by about a fifth when $R \approx 0.3\%$, so that the order-of-magnitude estimate is still valid. The streaks length, $\lambda_x = \mathcal{O}(1000)$ for fixed-wall conditions, is representative of the disturbance flow along the x-direction (Kline et al., 1967). Ricco (2004) has shown that λ_x decreases by about a third when $R \approx 0.3\%$. The order of magnitude of $\lambda_x = \mathcal{O}(1000)$ is therefore applicable under wall-oscillation conditions. The length scale along y for the mean flow is the spanwise boundary layer thickness δ, defined here as the distance from the wall where the maximum $\overline{U_z}$ equals $\exp(-1)U_{zm}$. As amply verified (see Choi et al. (2002), amongst many) $\overline{U_z}$ agrees well with the laminar solution of the second Stokes problem for the flow induced by wall oscillations beneath a still fluid (Batchelor, 1967), so that the spanwise boundary layer thickness can be approximated well by $\delta = \sqrt{T/\pi}$. For $T = 100$, $\delta \approx 5.7$, so that it can be assumed that $\delta = \mathcal{O}(10)$. The boundary layer thickness δ can be taken as the characteristic length scale for the near-wall disturbance flow because the oscillating boundary layer affects the turbulence in a region close to the wall whose width is comparable with δ. This is shown for example in figure 1.5 by the $\langle\overline{u_x u_y}\rangle$ profile being markedly affected only for $y < 25$ and by the $\overline{u_y u_z}$ profile reaching its maximum at $y \approx 15$. The mean-flow length scale becomes the length scale of the fluctuations along the direction of the shear also in other shear-driven phenomena, such as the penetration of free-stream turbulence into the Blasius boundary layer to form the Klebanoff modes (Leib et al., 1999). In that case, the wall-normal scale of the fluctuations within the boundary layer is the Blasius boundary layer thickness. The characteristic length scales along the Cartesian directions can therefore be taken as $\lambda_x > \lambda_z > \delta$.

As for the order of magnitude of the velocity components near the wall, as outlined by Pope (2000) at page 283, both u_x and u_z show a linear growth near the wall, but the coefficient is larger for the streamwise component. The wall-normal component u_y is smaller than both u_x and u_z because it grows quadratically from the wall. The hypothesis $u_x > u_z > u_y$ can therefore be adopted.

The order of magnitude of the enstrophy terms 3, 4 and 6, arising in (3.1) because of the wall oscillation, can now be estimated. The terminologies 'larger' and 'smaller' are to be intended in the order-of-magnitude sense. For brevity, the time-averaging symbol

is omitted to the end of §3.2.1. Term 3 can be first decomposed as follows.

$$\text{Term 3}: \quad \overline{\omega_z\omega_y}\overline{U_z}_{,y} = \left(\underbrace{\overline{u_{y,x}u_{x,z}}}_{3a} - \underbrace{\overline{u_{y,x}u_{z,x}}}_{3b} - \underbrace{\overline{u_{x,y}u_{x,z}}}_{3c} + \underbrace{\overline{u_{x,y}u_{z,x}}}_{3d} \right) \overline{U_z}_{,y}, \tag{3.2}$$

and the order of magnitude of each sub-term is

$$3a \sim \frac{u_x u_y}{\lambda_x \lambda_z}, 3b \sim \frac{u_y u_z}{\lambda_x^2}, 3c \sim \frac{u_x^2}{\delta \lambda_z}, 3d \sim \frac{u_x u_z}{\delta \lambda_x}, \overline{U_z}_{,y} \sim \frac{U_{zm}}{\delta}.$$

It is evident that term $3c$, $\overline{u_{x,y}u_{x,z}}\overline{U_z}_{,y}$, is dominant. It follows that

$$\text{Term 3}: \overline{\omega_z\omega_y}\overline{U_z}_{,y} = \mathcal{O}\left(\frac{u_x^2 U_{zm}}{\delta^2 \lambda_z} \right).$$

It further occurs that term $3d >$ term $3a >$ term $3b$. The magnitude of term 4 is estimated as follows.

$$\begin{aligned} \text{Term 4}: \quad \overline{\omega_i u_{x,i}}\overline{U_z}_{,y} &= \left[\overline{\left(u_{z,y} - u_{y,z}\right) u_{x,x}} + \overline{\left(u_{x,z} - u_{z,x}\right) u_{x,y}} + \overline{\left(u_{y,x} - u_{x,y}\right) u_{x,z}} \right] \overline{U_z}_{,y} \\ &= \left(\underbrace{\overline{u_{z,y}u_{x,x}}}_{4a} - \underbrace{\overline{u_{y,z}u_{x,x}}}_{4b} - \underbrace{\overline{u_{z,x}u_{x,y}}}_{4c} + \underbrace{\overline{u_{y,x}u_{x,z}}}_{4d} \right) \overline{U_z}_{,y}, \end{aligned}$$

$$4a, 4c \sim \frac{u_x u_z}{\delta \lambda_x}, \ 4b, 4d \sim \frac{u_x u_y}{\lambda_x \lambda_z}.$$

Terms $4a$ and $4c$ are larger than $4b$ and $4d$ because $u_z > u_y$ and $\delta < \lambda_z$, so that

$$\text{Term 4}: \overline{\omega_i u_{x,i}}\overline{U_z}_{,y} = \mathcal{O}\left(\frac{u_x u_z U_{zm}}{\delta^2 \lambda_x} \right). \tag{3.3}$$

Note that this represents an upper bound because terms $4a$ and $4c$ may add to produce a term of the order of magnitude given in (3.3) or give a term of smaller amplitude if these terms are of opposite sign. The magnitude of term 6 can be estimated as follows.

$$\text{Term 6}: \quad -\overline{u_y\omega_x}\overline{U_z}_{,yy} = \left(-\overline{u_y u_{z,y}} + \overline{u_y u_{y,z}} \right) \overline{U_z}_{,yy},$$

$$\overline{u_y u_{z,y}} \sim \frac{u_y u_z}{\delta}, \ \overline{u_y u_{y,z}} \sim \frac{u_y u_y}{\lambda_z}, \ \overline{U_z}_{,yy} \sim \frac{U_{zm}}{\delta^2}.$$

The term $-\overline{u_y u_{z,y}}\overline{U_z}_{,yy}$ is clearly dominant because $u_z > u_y$ and $\delta > \lambda_z$. It follows that

$$\text{Term 6}: -\overline{u_y\omega_x}\overline{U_z}_{,yy} = \mathcal{O}\left(\frac{u_y u_z U_{zm}}{\delta^3} \right).$$

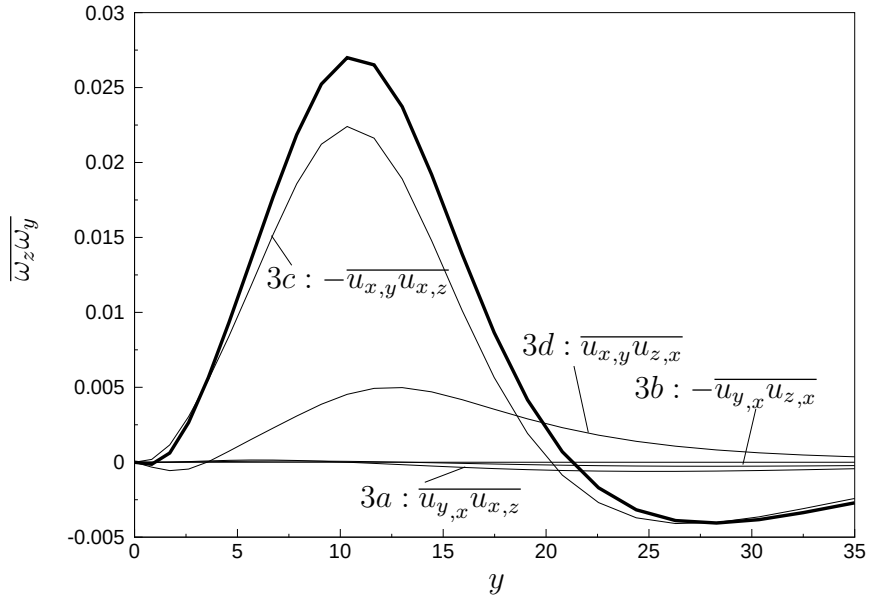

Figure 3.3: Wall-normal profile of $\overline{\omega_z\omega_y}$ for $T = 100$ at the phase at which it reaches its maximum (thick line). Thin lines indicate the sub-terms in (3.3).

In order to compare term 6 with term 3, we resort to the continuity equation, as follows

$$u_{y,y} \sim u_{x,x} \Longrightarrow \frac{u_y}{\delta} \sim \frac{u_x}{\lambda_x},$$

$$\text{Term 6} : -\overline{u_y\omega_x}\overline{U_z}_{,yy} = \mathcal{O}\left(\frac{u_y u_z U_{zm}}{\delta^3}\right) = \mathcal{O}\left(\frac{u_x u_z U_{zm}}{\delta^2\lambda_x}\right).$$

Since $u_x > u_z$ and $\lambda_x > \lambda_z$, one obtains

$$\text{Term 3} : \mathcal{O}\left(\frac{u_x^2 U_{zm}}{\delta^2\lambda_z}\right) > \text{Term 6} : \mathcal{O}\left(\frac{u_x u_z U_{zm}}{\delta^2\lambda_x}\right).$$

Terms 4 and 6 are either comparable, when the upper bound case for the order-of-magnitude estimate for term 4 is considered, or term 4 $<$ term 6 if the two comparable leading terms in 4 have opposite sign. It can be concluded that term 3 $>$ term 6 $\geq$ term 4, which is the result found through the numerical simulations.

3.2.2 Physical interpretation of $\left\langle\overline{\omega_z\omega_y}\overline{U_z}_{,y}\right\rangle$

Term 3 in the enstrophy equation (3.1), $\left\langle\overline{\omega_z\omega_y}\overline{U_z}_{,y}\right\rangle$, has been found to be dominant and largely responsible for the change of global turbulent enstrophy and thus for drag reduction. It is positive and therefore indicates a production of vorticity, i.e. the mean spanwise flow shear $\overline{U_z}_{,y}$ acts on the turbulence structures represented by the correlation

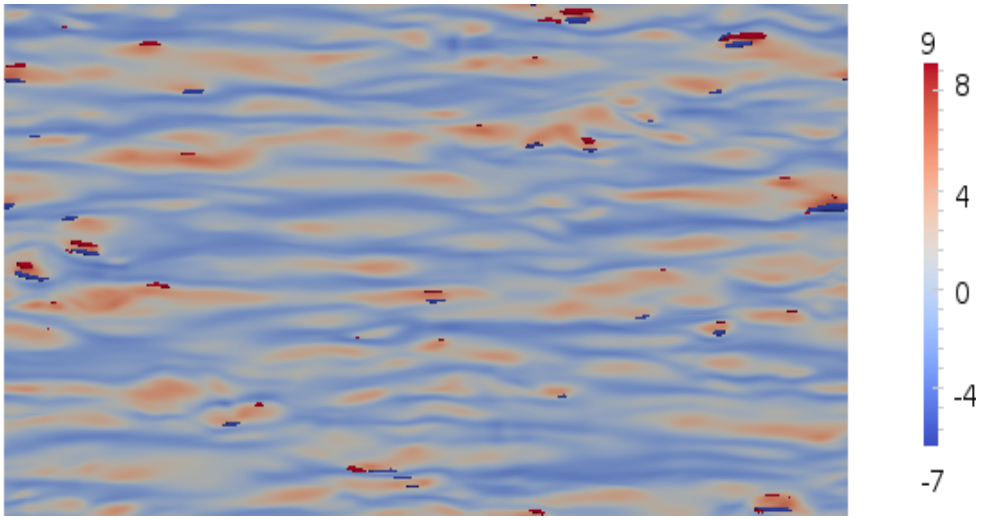

Figure 3.4: Colour map for streamwise velocity fluctuations for fixed-wall case in the $x-z$ plane at $y = 6$. Surfaces are for $u_{x,y}u_{x,z} > 1.25$ (dark red) and $u_{x,y}u_{x,z} < -1.25$ (dark blue).

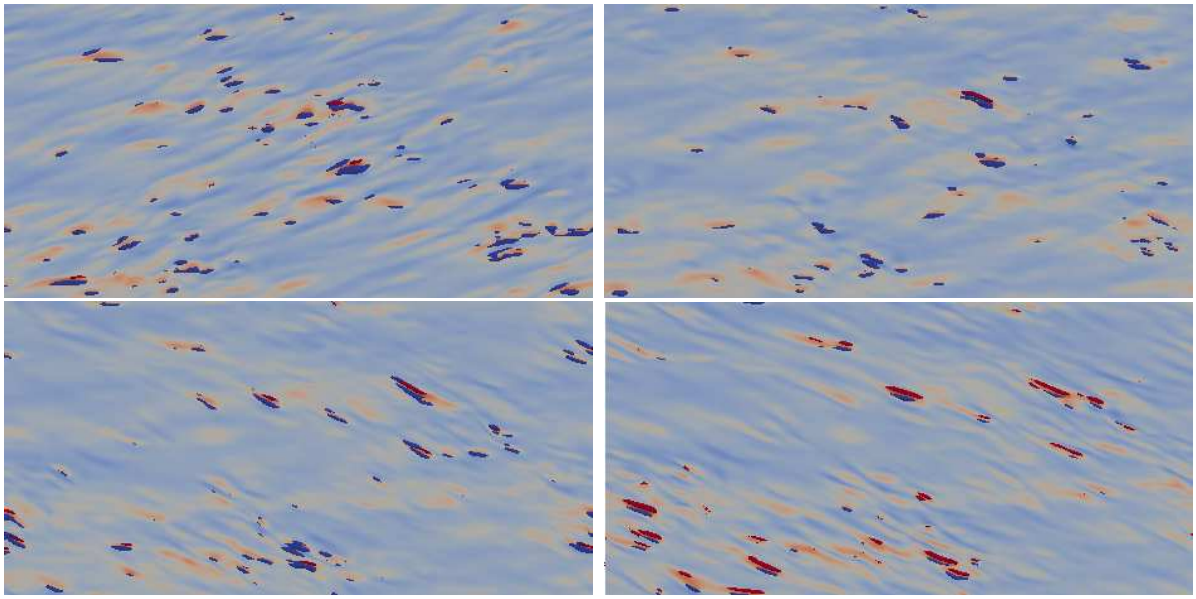

Figure 3.5: Surfaces at constant $u_{x,y}u_{x,z}$ and colour map for streamwise velocity fluctuations for oscillating-wall case ($T = 100$) in the $x - z$ plane at $y = 6$. Colour scales are the same of figure 3.4.

term $\overline{\omega_z \omega_y}$ to increase the turbulent enstrophy. This physical meaning of such interaction is investigated in more detail in this section.

Figure 3.3 confirms the result of the order-of-magnitude analysis in §3.2.1, i.e. that term 3*c*, $\overline{u_{x,y} u_{x,z}}$, is dominant amongst the ones composing $\overline{\omega_z \omega_y}$, and that the next subterm in magnitude is term 3*d*, $\overline{u_{x,y} u_{z,x}}$. Terms $u_{x,z}$ and $u_{x,y}$ may be linked separately to the dynamics of the turbulent low-speed streaks. In the near-wall region, $u_{x,z}$ denotes the spanwise gradient of the low-speed streaks and it is maximum at their edge, i.e. at the interface of the low-velocity and high-velocity regions. Lee and Kim (2002) indeed state that the streaks are associated with fluctuations of wall-normal vorticity. The wall-normal gradient $u_{x,y}$ may instead be interpreted as the eruption of near-wall low-speed structures to higher locations or as sweep-like motion of high-speed fluid toward the wall. In order to understand the meaning of the product of the two quantities, we resort to flow visualizations. Figure 3.4 shows contour plots of streamwise velocity fluctuations u_x (light contours) and of the correlation $u_{x,y} u_{x,z}$ (dark contours) over the $x - z$ plane at $y = 6$ for the reference case. Low- and high-speed streaks show the characteristic streamwise-stretched shape. Low-speed ones are longer and thinner than the high-speed ones. Regions of high magnitude of the correlation appear sporadically and always occur at the side of the high-speed streaks. Figure 3.5 shows the contours plots for the oscillating-wall case at four different phases, where the characteristic cyclic tilting of the near-wall structures is evident (Quadrio and Ricco, 2003). The streaks are less energetic, which confirms the attenuation of u_{xrms}, shown in figure 1.5. The number, the amplitude and the spatial size of the $u_{x,y} u_{x,z}$ pockets increases during the wall motion, in line with the observed intensified enstrophy fluctuations.

Further insight may be gained by a model of the turbulent enstrophy transport, following Davidson (2004) at pages 211, 213 and 263, and other analogous studies focussed on the passive scalar transport in a turbulent flow (Bouremel et al., 2009a,b). The approach is similar to the rapid distortion theory problem of a large eddy stretching a smaller blob of vorticity, presented at page 213 in Davidson (2004). Analogously, we consider here small-scale vorticity structures being continuously stretched, compressed and transported by the large-scale action of the Stokes layer. It is assumed that the energy associated with the small-scale motion is much smaller than the one of the large-scale forcing, the Stokes layer is quasi-steady with respect to the small-scale fluctuations, its action is inviscid, and its gradient is uniform on the scale of the small motions. The contribution of the wall motion to the enstrophy production may thus be distilled into the following simplified enstrophy equation in the $y - z$ plane

$$\frac{1}{2} \left(\omega_y^2 + \omega_z^2 \right)_{,t} = \omega_z \omega_y U_{z,y}, \tag{3.4}$$

where ω_y and ω_z are to be intended here as turbulent vorticity fluctuations which are smaller than the spatial scale at which the Stokes layer operates. The term on the r.h.s. of (3.4) may be written in matrix form as follows

$$\omega_z \omega_y U_{z,y} = [\omega_y ; \omega_z] \frac{1}{2} \begin{bmatrix} 0 & U_{z,y} \\ U_{z,y} & 0 \end{bmatrix} \begin{bmatrix} \omega_y \\ \omega_z \end{bmatrix}.$$

In order to elucidate the mechanism of vorticity production, a set of perpendicular axes

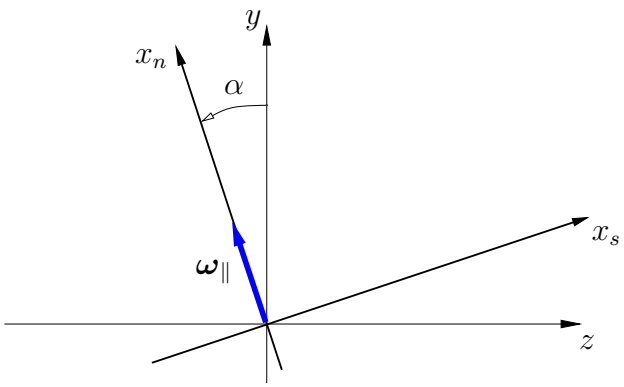

Figure 3.6: Coordinate systems in $y-z$ plane for turbulent vorticity vector $\boldsymbol{\omega}_\parallel$.

(x_n, x_s) may be considered where x_n is orientated along the vorticity vector in the $y-z$ plane, $\boldsymbol{\omega}_\parallel = [\omega_y; \omega_z]$. The angle α is defined as the angle between $\boldsymbol{\omega}_\parallel$ and the wall-normal axis y, as shown in figure 3.6. Upon considering the new set of coordinates, the production term is written as

$$\omega_z \omega_y U_{z,y} = [\omega_n; 0] \begin{bmatrix} S_{nn} & S_{ns} \\ S_{sn} & S_{ss} \end{bmatrix} \begin{bmatrix} \omega_n \\ 0 \end{bmatrix} = S_{nn} \omega_n^2,$$

where $S_{nn} = \sin\alpha \cos\alpha U_{z,y}$ and $\omega_n^2 = \omega_y^2 + \omega_z^2$. The other components of the strain-rate tensor S_{ns}, S_{sn}, S_{ss} only contribute to change the direction of the vorticity vector, not its magnitude. Equation (3.4) may be integrated to give

$$\omega_n^2 = (\omega_n)_0^2 \exp\left(2 \sin\alpha \cos\alpha \, U_{z,y} t\right), \tag{3.5}$$

where $(\omega_n)_0^2$ is the initial magnitude. Equation (3.5) shows that the Stokes layer may generate or attenuate the local enstrophy depending on the sign of its gradient and the orientation of the vorticity vector. Turbulent enstrophy production by stretching occurs when $\sin\alpha \cos\alpha \, U_{z,y} > 0$, and the rate of growth or decay of enstrophy is never larger than $U_{z,y}$. The rate of change is null when the vorticity vector is parallel or perpendicular to the wall, and the maximum enstrophy production occurs when either i) $U_{z,y}$ is at its negative peak at that y location and simultaneously $\boldsymbol{\omega}_\parallel$ is orientated at $\pi/2$ with respect to the axes and along the first or third quadrant in figure 3.6, or ii) $U_{z,y}$ is at its positive peak and simultaneously $\boldsymbol{\omega}_\parallel$ is orientated at $\pi/2$ with respect to the axes and along the second or fourth quadrant in figure 3.6.

3.2.3 Turbulent energy dissipation balance

We close this section by pointing out that the transport equation for the turbulent energy dissipation could have been used in lieu of the turbulent enstrophy equation (3.1).

The transport equation for the turbulent energy dissipation, called ϵ here

$$\epsilon \equiv \overline{u_{i,j}(u_{i,j} + u_{j,i})},$$

is studied (Mansour et al., 1989; Fischer et al., 2001). For the case of turbulent channel flow with spanwise wall oscillations, the equation reads

$$\begin{aligned}\underbrace{\epsilon_{,t}/2}_{1} = &-\underbrace{\overline{u_{x,i}u_{y,i}}\,\overline{U}_{x,y}}_{2} = -\underbrace{\overline{u_{z,i}u_{y,i}}\,\overline{U}_{z,y}}_{3} - \underbrace{\overline{u_{i,x}u_{i,y}}\,\overline{U}_{x,y}}_{4} - \underbrace{\overline{u_{i,z}u_{i,y}}\,\overline{U}_{z,y}}_{5} - \underbrace{\overline{u_y u_{x,y}}\,\overline{U}_{x,yy}}_{6} \\ &- \underbrace{\overline{u_y u_{z,y}}\,\overline{U}_{z,yy}}_{7} - \underbrace{\overline{u_{i,k}u_{j,k}u_{i,j}}}_{8} - \underbrace{\left(\overline{u_y u_{i,j}u_{i,j}}\right)_{,y}/2}_{9} - \underbrace{\overline{u_{i,j}p_{,ij}}}_{10} - \underbrace{\overline{u_{i,jk}u_{i,jk}}}_{11} + \underbrace{\epsilon_{,yy}}_{12}.\end{aligned} \tag{3.6}$$

The turbulent dissipation equation has a form similar to the enstrophy one. The order of magnitude of the terms arising in (3.6) because of the wall motion can be estimated through an analysis similar to one for the enstrophy equation (3.1). The magnitude of term 3 is found as follows.

$$\text{Term 3}: \quad \overline{u_{z,i}u_{y,i}}\,\overline{U}_{z,y} = \left(\underbrace{\overline{u_{z,x}u_{y,x}}}_{3a} + \underbrace{\overline{u_{z,y}u_{y,y}}}_{3b} + \underbrace{\overline{u_{z,z}u_{y,z}}}_{3c}\right)\overline{U}_{z,y}, \tag{3.7}$$

$$3a \sim \frac{u_y u_z}{\lambda_x^2},\ 3b \sim \frac{u_y u_z}{\delta^2} \sim \frac{u_x u_z}{\lambda_x \delta},\ 3c \sim \frac{u_y u_z}{\lambda_z^2} \sim \frac{u_y u_x}{\lambda_z \lambda_x},\ \overline{U}_{z,y} \sim \frac{U_{zm}}{\delta}.$$

Term $3b$ is dominant, so that

$$\text{Term 3}: \overline{u_{z,i}u_{y,i}}\,\overline{U}_{z,y} = \mathcal{O}\left(\frac{u_x u_z U_{zm}}{\delta^2 \lambda_x}\right).$$

The magnitude of term 5 is estimated as follows.

$$\text{Term 5}: \quad \overline{u_{i,z}u_{i,y}}\,\overline{U}_{z,y} = \left(\underbrace{\overline{u_{x,z}u_{x,y}}}_{5a} + \underbrace{\overline{u_{y,z}u_{y,y}}}_{5b} + \underbrace{\overline{u_{z,z}u_{z,y}}}_{5c}\right)\overline{U}_{z,y}, \tag{3.8}$$

$$5a \sim \frac{u_x^2}{\delta \lambda_z},\ 5b \sim \frac{u_y^2}{\delta \lambda_z},\ 5c \sim \frac{u_z^2}{\delta \lambda_z}.$$

Term $5a$ is dominant. It follows that

$$\text{Term 5}: \overline{u_{i,z}u_{i,y}}\,\overline{U}_{z,y} = \mathcal{O}\left(\frac{u_x^2 U_{zm}}{\delta^2 \lambda_z}\right).$$

The magnitude of term 7 is found as follows.

$$\text{Term 7}: \quad \overline{u_y u_{z,y}}\,\overline{U}_{z,yy}, \tag{3.9}$$

$$\overline{u_y u_{z,y}} \sim \frac{u_y u_z}{\delta} \sim \frac{u_x u_z}{\lambda_x},\ \overline{U}_{z,yy} \sim \frac{U_{zm}}{\delta^2},$$

$$\text{Term 7}: \overline{u_y u_{z,y}}\,\overline{U}_{z,yy} = \mathcal{O}\left(\frac{u_x u_z U_{zm}}{\delta^2 \lambda_x}\right).$$

Term 5a is estimated to be the largest one amongst the terms in (3.6) induced by the wall motion. This result confirms the analysis of the turbulent enstrophy equation (3.1) in §3.2, where term 3, of the same order of magnitude, emerges as dominant and significantly modifies the balance.

Chapter 4

Prediction of turbulent drag reduction

As a consequence of the results found in §3, it follows a number of considerations about the scaling of drag reduciton to the aim of clarifying the physical mechanism and predicting R.

4.1 Drag reduction and $\overline{\omega_z\omega_y}\overline{U_{z,y}}$

In this section, the focus is on the relationship between R and term 3 in (3.1), $\overline{\omega_z\omega_y}\overline{U_{z,y}}$. In line with the finding that $\overline{\omega_z\omega_y}\overline{U_{z,y}}$ is the main responsible factor for the turbulent enstrophy change, and therefore for the C_f reduction, figure 4.1 shows that R scales linearly with the global value of $\overline{\omega_z\omega_y}\overline{U_{z,y}}$ up to $R \approx 0.3\%$, which corresponds to $T = 42$. The global value of the enstrophic term is chosen here because R is linked via (1.9) to the change of U_b, a global quantity as defined in (1.8). After the linear growth the relationship between these two terms is not linear anymore and this negative behaviour get worse with the period. For very high periods term three is not dominant in the enstrophy balance and the relationship with R is lost. This is the most important result of the entire work. Figure 4.2 further reveals that the global term relates linearly with $\sqrt{T}$ up to conditions exceeding the optimum.

4.2 An analyticl formula to predict R

Prompted by these results, the objective is now to model the global value of $\overline{\omega_z\omega_y}\overline{U_{z,y}}$ by analytic expressions in order to extract a parameter $S = S(T; U_{zm})$, which relates to R. An analytical formula for R can be a useful tool to experimentalists for design purposes. The parameter is therefore as follows

$$S = S(T; U_{zm}) = \int_0^h \left\langle \overline{\omega_z\omega_y}\overline{U_{z,y}} \right\rangle \mathrm{d}y. \tag{4.1}$$

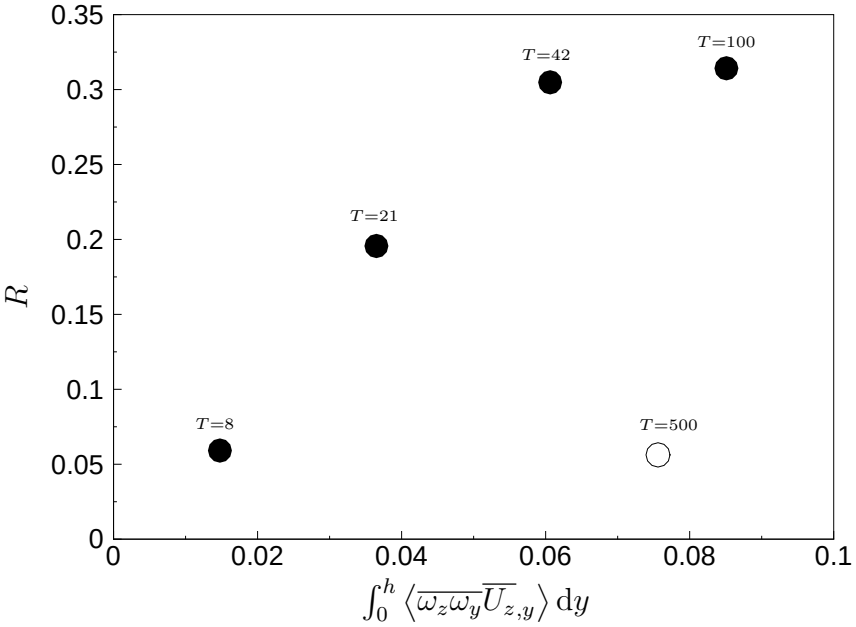

Figure 4.1: Drag reduction rate R vs. global term $\int_0^h \langle \overline{\omega_z \omega_y} \overline{U_z}_{,y} \rangle \, \mathrm{d}y$.

The aim is to predict R for as high values of T as possible. However, R and the global enstrophic term are related linearly only up to $T \approx 42 < T_{opt}$, whereas, at higher periods, the enstrophic term is larger than what it would be if the linear correlation were valid, as shown in figure 4.1 (left). This suggests that, in order to extract a linear correlation between S and R for conditions up to (or exceeding) the optimal ones, the enstrophic term should be modelled accurately up to $T \approx 42$, and it should be suitably underestimated by the model at higher periods. This prediction, based solely on observation of the numerical data shown in figure 4.1, will be confirmed as accurate once the scaling function is extracted.

The modelling of $\overline{\omega_z \omega_y}$ is carried out as follows. Figure 4.3 (left) shows its wall-normal profiles at different phases for $T = 21$. The vorticity fluctuations do not penetrate through a very thin near-wall layer, $y < y_s \approx 2$. For $y > y_s$, the correlation grows linearly up to a maximum and then decays as y increases. The correlation shares the frequency-shift behaviour of the wall-normal profile of $\overline{U_z}$ at different heights. A formula which captures well the correlation profile is therefore

$$\overline{\omega_z \omega_y} = \begin{cases} 0, y < y_s, \\ \phi \left(y - y_s \right) \exp \left[-\gamma \left(y - y_s \right) \right] \cos \left[\frac{2\pi t}{T} - \gamma \left(y - y_s \right) \right], y \geq y_s, \end{cases} \tag{4.2}$$

where $\gamma = \gamma(T)$ and $\phi = \phi(T)$ model the peak correlation value $C_m(T)$ and its position $y_m(T)$. For small T, C_m and $y_m(T) - y_s$ grow as $\sim \sqrt{T}$, while, at large T, they tend asymptotically to constant values, C_{opt} and $\tilde{y} = y_{opt} - y_s$, respectively. The trends are

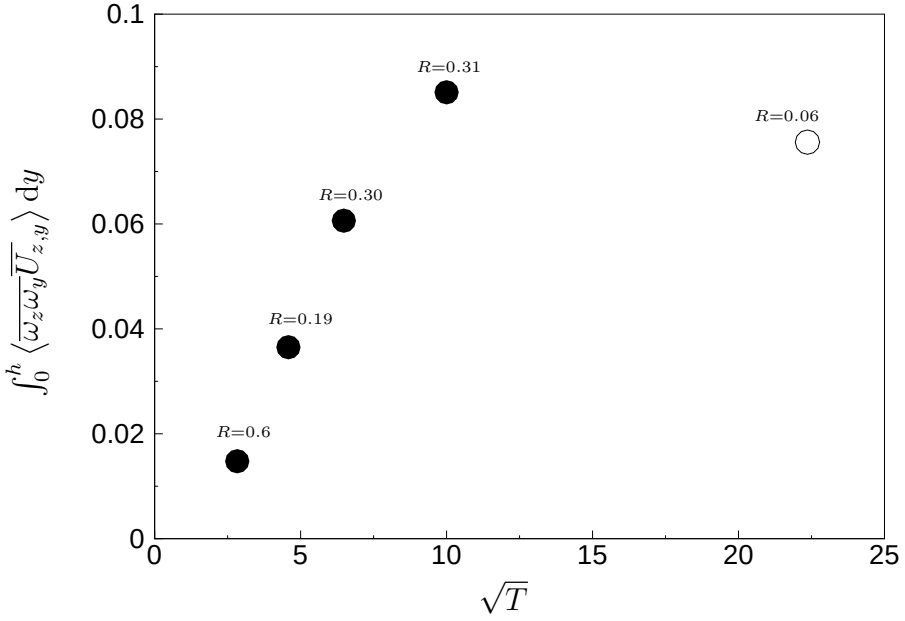

Figure 4.2: Global term $\int_0^h \left\langle \overline{\omega_z \omega_y} \overline{U}_{z,y} \right\rangle \mathrm{d}y$ vs. $\sqrt{T}$.

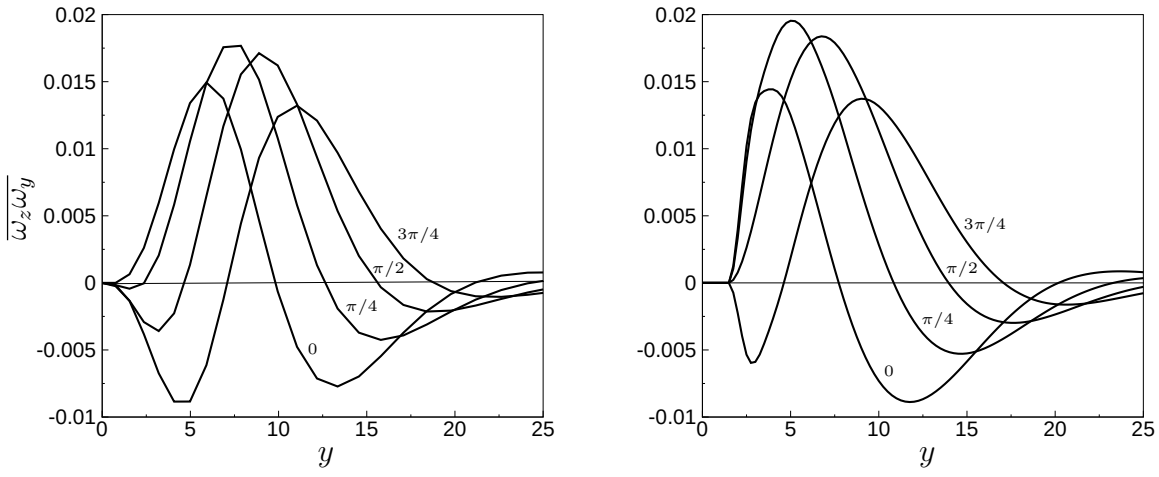

Figure 4.3: Wall-normal DNS profiles of $\overline{\omega_z \omega_y}$ at different phases for $T = 21$ (left) and corresponding model profiles (right), calculated with the free parameters in (4.2) that minimize the difference between the amount of drag reduction calculated via DNS and the modelled data (refer to discussion in the text).

thus represented well by the following

$$y_m(T) = y_s + \tilde{y}\left[\frac{2\arctan(\alpha T)}{\pi}\right]^{1/2}, \quad C_m(T) = C_{opt}\left[\frac{2\arctan(\beta T)}{\pi}\right]^{1/2}. \tag{4.3}$$

By differentiating the envelope of the model correlation (4.2), it is found that $\gamma = (y_m - y_s)^{-1}$, and $\phi = e\gamma C_m$. The constants $\alpha, \beta, y_{opt}, C_{opt}, y_s$ will be found later by best fitting of the numerical R data.

The spanwise flow $\overline{U_z}$ is modelled by the Stokes problem laminar solution of the flow engendered by sinusoidal wall oscillations beneath a still fluid (Batchelor, 1967). As verified by Quadrio and Sibilla (2000) and Choi et al. (2002), the laminar solution approximates well the mean spanwise flow for $T < T_{opt}$ at constant mass flux, i.e. for $T < 150$. Ricco and Quadrio (2008) showed that the discrepancy between the two flows is due to the additional term $\overline{u_y u_z}_{,y}$ in the turbulent z-momentum equation with respect to the corresponding laminar equation. For $T = 125$, its magnitude has been shown to be significant during the initial temporal transient but negligible once the new regime has established. This has been further verified in §2.1.3 by the terms $\mathcal{S}_w$ and $\mathcal{D}_{U_z}$ (which coincide in the laminar case) being different by only 1% for $T = 100$. It is therefore assumed that

$$\overline{U_z} = U_{zm}\exp\left(-y\sqrt{\frac{\pi}{T}}\right)\cos\left(\frac{2\pi}{T}t - y\sqrt{\frac{\pi}{T}}\right). \tag{4.4}$$

For $T \approx 100$, the spanwise boundary layer thickness $\delta = \sqrt{T/\pi}$ is much smaller than the half-width of the channel, $h = 200$. The latter condition is necessary because solution (4.4) is valid for a semi-infinite domain bounded only by one oscillating wall. It further follows that the upper limit of the integral in (4.1) can be replaced by ∞.

The quantity S is obtained by substituting (4.2) and (4.4) into (4.1), as follows

$$S(T; U_{zm}) = \frac{U_{zm}\pi\phi T^{1/2}}{4\left(\pi + \gamma^2 T\right)^2}\left[\left(\pi + 2\gamma\sqrt{\pi T} - \gamma^2 T\right)\Re\left(\Psi\right) + \left(\pi - 2\gamma\sqrt{\pi T} - \gamma^2 T\right)\Im\left(\Psi\right)\right], \tag{4.5}$$

where $\Psi = \exp\left(-y_s\sqrt{2\pi i/T}\right)$ and $\Re$ and $\Im$ indicate the real and imaginary parts. The quantity S relates linearly with R up to $T \approx 100$ when the free parameters $\alpha, \beta, y_{opt}, C_{opt}$ and y_s are chosen so as to minimize the difference between the numerical R data and the data estimated through the model, i.e. $R_s = kS$, where k is a constant. It is found that $\alpha = 0.13$, $\beta = 0.03$, $y_{opt} = 6$, $C_{opt} = 0.033$, $y_s = 1.5$ and $k = 57.14286$. Figure 4.3 (right) depicts the model of $\overline{\omega_z\omega_y}$ at different phases for these values of the parameters. Figure 4.4 shows the excellent agreement between R and R_s up to $T \approx 100$ (solid line), which is further evidenced by their linear correlation in the right graph. The minimal period to obtain drag reduction, $T_{min} \approx 3$, is defined as the period where $S = 0$.

4.3 A brief discussion on the dependence of R on T

At very small periods, i.e. $T \leq T_{min}$, the friction drag is unchanged with respect to the fixed-wall case, as shown in figures 4.4 and 4.5. The layer where $\overline{U_z}$ is at work is so

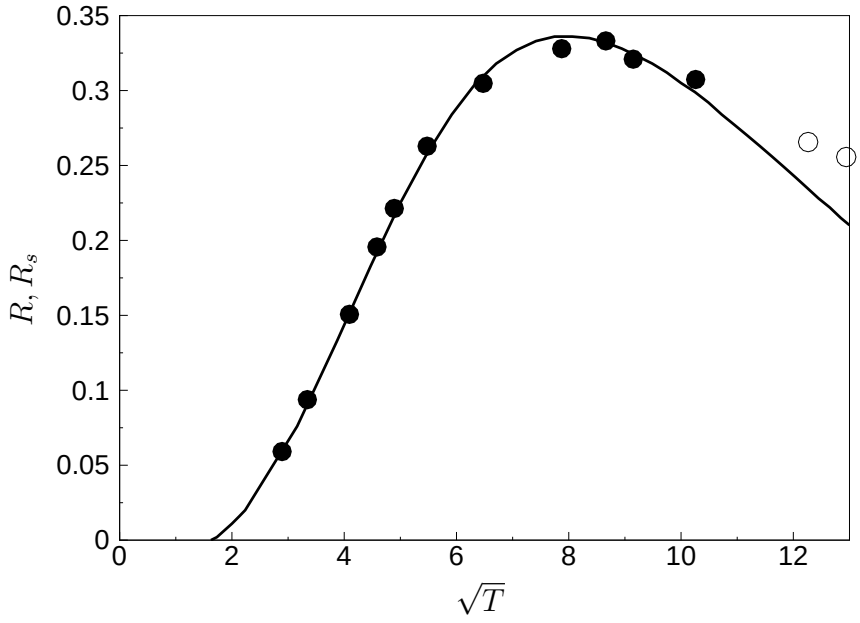

Figure 4.4: R data calculated via DNS (symbols) and $R_s = kS$, computed through S given by (4.5) (line), as functions of $\sqrt{T}$. Black circles are for $T \leq 100$, white circles are for $T > 100$

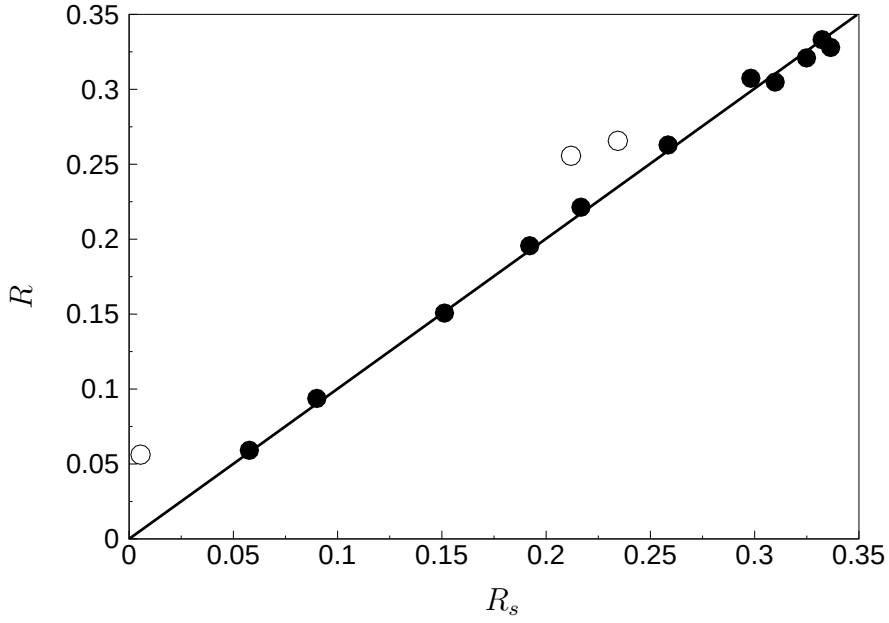

Figure 4.5: R vs. R_s; black circles are for $T \leq 100$, white circles are for $T > 100$; straight line is $R = R_s$.

thin ($\delta \leq \sqrt{T_{min}/\pi} \approx 1$) that its viscous effects do not diffuse sufficiently through the interior of the channel to affect the near-wall turbulence. As $\overline{\omega_z \omega_y}$ is negligibly small for $y < 1$, the production term $\overline{\omega_z \omega_y}\overline{U_z}_{,y}$ is not large enough to alter the turbulent enstrophy balance. The friction coefficient C_f is therefore unvaried.

For $T_{min} < T < T_{opt}$, both $\overline{\omega_z \omega_y}\overline{U_z}_{,y}$ and R grow as $\sqrt{T}$, i.e. $R \sim \delta$, as shown in figure 4.1 and 4.2. The Stokes layer is thick enough for $\overline{\omega_z \omega_y}\overline{U_z}_{,y}$ to influence the enstrophy balance. The spanwise viscous effects act only on the near-wall portion of $\overline{\omega_z \omega_y}$, which suggests that a crude approximation can be $\overline{\omega_z \omega_y} = (y - y_s)\cos(2\pi t/T)$. Substitution of the latter into (4.1) indeed leads to $R_s \sim \sqrt{T}$.

For T comparable with T_{opt}, the viscous effects engendered by $\overline{U_z}$ penetrate farther into the turbulent flow. The correlation $\overline{\omega_z \omega_y}$ is modelled by (4.2) because the Stokes layer is thick enough to affect the structures along their whole wall-normal extent. The prediction R_s is much less accurate for $T > T_{opt}$. For $T > 1000$, the flow is highly three-dimensional and quasi-steady and drag increase occurs (Quadrio et al., 2009). It would be of interest to explore the turbulent enstrophy balance for drag-increase conditions.

4.4 A note on the scaling parameter by Quadrio and Ricco (2004)

In this section, a conceptual link is proposed between the scaling factor found in the present work and the parameter employed by Choi et al. (2002) and discovered by Quadrio and Ricco (2004) to be related linearly to the amount of skin-friction reduction for periods of oscillations smaller or comparable with the optimum. This scaling parameter was constructed by combining a characteristic length scale related to the wall-normal distance at which the wall motion affects the turbulent structures and the maximum spanwise acceleration of the Stokes layer. It reads:

$$S = 2\sqrt{\frac{\pi}{T}} \ln\left(\frac{U_{zm}}{U_{zth}}\right) \exp\left(-\hat{y}\sqrt{\frac{2\pi}{T}}\right)$$

where $U_{zth} \approx 1.2$ is a threshold velocity and $\hat{y} \approx 6.3$ is a wall-normal distance representative of the diffusion of the Stokes-layer viscous effects. The first interesting observation is that such parameter can be written as follows:

$$S = \frac{2}{U_{zm}} \ln\left(\frac{U_{zm}}{U_{zth}}\right) \Omega_{xm}(\hat{y}), \tag{4.6}$$

where Ω_{xm} is the maximum streamwise vorticity of the Stokes layer at $y = \hat{y}$. Relation (4.6) endows the scaling parameter with a more direct and physically relevant meaning, in that it simply states that the drag reduction is linearly proportional to the maximum spanwise shear induced by the Stokes layer at constant U_{zm}, and that such shear is most effective when at work at $y \approx 6.3$.

The fact that the parameter used by Quadrio and Ricco (2004) relates well with drag reduction is not surprising in view of the scaling analysis previously presented. Indeed,

(4.6) can be seen as a very simplified version of the new scaling factor (4.1). Although the parameter (4.1) is more elaborate as it possesses a precise physical meaning and involves averaging and wall-normal integration, the spanwise shear of the Stokes layer plays a key role in both expressions. The other point of note is that $\left\langle \overline{\omega_z \omega_y} \overline{U_z}_{,y} \right\rangle$ reaches its maximum at $y \approx 6.5$ for optimum conditions for R, i.e. almost at the same distance at which the correlation between R and the parameter (4.6) is maximum.

Chapter 5

Conclusions

With the aim of understanding the turbulent drag reduction phenomenology, the physics of an incompressible turbulent channel flow, driven by a constant streamwise pressure gradient and modified by spanwise wall oscillations, has been studied by direct numerical simulations. The main effect of the oscillation is the increment of the bulk streamwise velocity, which translates in a reduction of the skin-friction coefficient. The energy spent to drive the wall motion almost coincides with the viscous dissipation of the large-scale spanwise motion, the difference taking the form of a small turbulence kinetic energy production term. The energy balance elucidates that the increase of the streamwise-flow kinetic energy is mainly balanced by the viscous dissipation associated with the mean streamwise flow and by the dissipation related to the turbulent fluctuations.

The oscillating spanwise boundary layer has a direct effect only on the latter, which can be conveniently expressed as the volume integral of the turbulent enstrophy. The study of transport equation for the turbulent enstrophy reveals that a single enstrophy production term synthesizes the stretching of the vorticity lines by the oscillating layer and it is therefore responsible for the increase of bulk velocity. Although the turbulent enstrophy increases, the intensity of the turbulent fluctuations decreases in the proximity of the wall. The amount of drag reduction relates linearly with square root of the period of oscillation and with the new enstrophy production term at small periods. A simple analytical model of such term has led to an analytical formula for prediction of drag reduction.

The present work has shown the importance of studying the turbulent enstrophy budget in order to gain a deeper understanding of turbulent drag reduction by spanwise wall oscillation. Arguably, the present method could be adopted to investigate other turbulent flows modified by external agents, such as boundary layers affected by large-scale Lorentz or Coriolis forces, by wall transpiration, by large temperature gradients, or by the addition of bubbles and polymeric solutions.

Bibliography

H. Abe, R.A. Antonia, and H. Kawamura. Correlation between small-scale velocity and scalar fluctuations in a turbulent channel flow. *J. Fluid Mech.*, 627:1–32, 2009.

R.A. Antonia and J. Kim. Low-Reynolds-number effects on near-wall turbulence. *J. Fluid Mech.*, 276:61–80, 1994.

G. K. Batchelor. *An Introduction to Fluid Dynamics*. Cambridge University Press, 1967.

T. W. Berger, J. Kim, C. Lee, and J. Lim. Turbulent boundary layer control utilizing the Lorentz force. *Phys. Fluids*, 12(3):631–649, 2000.

T. Bewley, P. Moin, and R. Temam. DNS-based predictive control of turbulence: an optimal benchmark for feedback algorithms. *J. Fluid Mech.*, 447:179–225, 2001.

Y. Bouremel, M. Yianneskis, and A. Ducci. On the utilisation of vorticity and strain dynamics for improved analysis of stirred processes. *Chem. Eng. Res. Design*, 87: 377–385, 2009a.

Y. Bouremel, M. Yianneskis, and A. Ducci. Three-dimensional deformation of trailing vortex structures in a stirred vessel. *Ind. Eng. Chem. Res.*, 48(17):8148–8158, 2009b.

P. Bradshaw and N.S. Pontikos. Measurements in the turbulent boundary layer on an 'infinite' swept wing. *J. Fluid Mech.*, 159:105–130, 1985.

J-I. Choi, C.-X. Xu, and H. J. Sung. Drag reduction by spanwise wall oscillation in wall-bounded turbulent flows. *AIAA J.*, 40(5):842–850, 2002.

K.-S. Choi. Near-wall structure of a turbulent boundary layer with riblets. *Journal of Fluid Mechanics*, 208:417–458, 1989.

K.-S. Choi. Near-wall structure of turbulent boundary layer with spanwise-wall oscillation. *Phys. Fluids*, 14(7):2530–2542, 2002.

K-S. Choi and M. Graham. Drag reduction of turbulent pipe flows by circular-wall oscillation. *Phys. Fluids*, 10(1):7–9, 1998.

K-S. Choi, J.R. DeBisschop, and B.R. Clayton. Turbulent boundary-layer control by means of spanwise-wall oscillation. *AIAA J.*, 36(7):1157–1162, 1998.

G. N. Coleman, J. Kim, and A. T. Le. A numerical study of three-dimensional wall-bounded flows. *Int. J. Heat Fluid Flow*, 17:333–342, 1996.

P.A. Davidson. *Turbulence: An Introduction for Scientists and Engineers*. Oxford University Press, 2004.

M.R. Dhanak and C. Si. On reduction of turbulent wall friction through spanwise oscillations. *J. Fluid Mech.*, 383:175–195, 1999.

Y. Du and G. E. Karniadakis. Suppressing Wall Turbulence by Means of a Transverse Traveling Wave. *Science*, 288:1230–1234, 2000.

Y. Du, V. Symeonidis, and G. E. Karniadakis. Drag reduction in wall-bounded turbulence via a transverse travelling wave. *J. Fluid Mech.*, 457:1–34, 2002.

M. Fischer, J. Jovanović, and F. Durst. Reynolds number effect in the near-wall region of turbulent channel flow. *Phys. Fluids*, 13(6):1755–1767, 2001.

B. Frohnapfel, J. Jovanovic, and A. Delgado. Experimental investigation of turbulent drag reduction by surface-embedded grooves. *J. Fluid Mech.*, 590:107–116, 2007.

J.J. Gorski, J.M. Wallace, and P.S. Bernard. The enstrophy equation budget of bounded turbulent shear flows. *Phys. Fluids*, 6(9):3197–3199, 1994.

J. O. Hinze. *Turbulence*. McGraw Hill – Second Edition, 1975.

M. Itoh, S. Tamano, K. Yokota, and S. Taniguchi. Drag reduction in a turbulent boundary layer on a flexible sheet undergoing a spanwise traveling wave motion. *J. Turbulence*, 7(27):1–17, 2006.

K. Iwamoto, Y. Suzuki, and N. Kasagi. Reynolds number effect on wall turbulence: toward effective feedback control. *Int. J. Heat Fluid Flow*, 23:678–689, 2002.

W.J. Jung, N. Mangiavacchi, and R. Akhavan. Suppression of turbulence in wall-bounded flows by high-frequency spanwise oscillations. *Phys. Fluids A*, 4 (8):1605–1607, 1992.

N. Kasagi, Y. Hasegawa, and K. Fukagata. Towards cost-effective control of wall turbulence for skin-friction drag reduction. In B. Eckhardt, editor, *Advances in Turbulence XII, Proc. 12th EUROMECH Eur. Turbul. Conf.*, volume 132. Springer Proceedings in Physics, 2009a.

N. Kasagi, Y. Suzuki, and K. Fukagata. Microelectromechanical systems-based feedback control of turbulence for drag reduction. *Annu. Rev. Fluid Mech.*, 41:231–251, 2009b.

J. Kim and T.R. Bewley. A Linear Systems Approach to Flow Control. *Annu. Rev. Fluid Mech.*, 39:383–417, 2007.

S. J. Kline, W. C. Reynolds, F. A. Schraub, and P. W. Runstadler. The structure of turbulent boundary layers. *J. Fluid Mech.*, 30:741–773, 1967.

F. Laadhari. Reynolds number effect on the dissipation function in wall-bounded flows. *Phys. Fluids*, 19(038101), 2007.

F. Laadhari, L. Skandaji, and R. Morel. Turbulence reduction in a boundary layer by a local spanwise oscillating surface. *Phys. Fluids*, 6 (10):3218–3220, 1994.

C. Lee and J. Kim. Control of viscous sublayer for drag reduction. *Phys. Fluids*, 14(7): 2523–2529, 2002.

S. J. Leib, D. W. Wundrow, and M. E. Goldstein. Effect of free-stream turbulence and other vortical disturbances on a laminar boundary layer. *J. Fluid Mech.*, 380:169–203, 1999.

P. Luchini and M. Quadrio. A low-cost parallel implementation of direct numerical simulation of wall turbulence. *J. Comp. Phys.*, 211(2):551–571, 2006.

N.N. Mansour, J. Kim, and P. Moin. Near-Wall $\kappa - \epsilon$ Turbulence Modeling. *AIAA J.*, 27(8):1068–1073, 1989.

T. Min, S.M. Kang, J.L. Speyer, and J. Kim. Sustained sub-laminar drag in a fully developed channel flow. *J. Fluid Mech.*, 558:309–318, 2006.

Y. Mito and N. Kasagi. DNS study of turbulence modification with streamwise-uniform sinusoidal wall-oscillation. *Int. J. Heat Fluid Flow*, 19(5):470–481, 1998.

J. Pang and K.-S. Choi. Turbulent drag reduction by Lorentz force oscillation. *Phys. Fluids*, 16(5):L35–L38, 2004.

S.B. Pope. *Turbulent Flows*. Cambridge University Press, Cambridge, 2000.

M. Quadrio. Drag-reducing characteristics of the generalized spanwise Stokes layer: experiments and numerical simulations. In *International Specialist Workshop on Open-Loop versus Closed-Loop Control of Wall Turbulence*. March 17–19, Tokyo (JP), 2010a.

M. Quadrio. Drag reduction in turbulent boundary layers by in-plane wall motion. *Royal Society Phil. Transactions A*, 2010b. Invited contribution. In press.

M. Quadrio and P. Ricco. Initial response of a turbulent channel flow to spanwise oscillation of the walls. *J. Turbulence*, 4(7), 2003.

M. Quadrio and P. Ricco. Critical assessment of turbulent drag reduction through spanwise wall oscillation. *J. Fluid Mech.*, 521:251–271, 2004.

M. Quadrio and P. Ricco. The laminar generalized Stokes layer and turbulent drag reduction. *Submitted to J. Fluid Mech.*, 2010.

M. Quadrio and S. Sibilla. Numerical simulation of turbulent flow in a pipe oscillating around its axis. *J. Fluid Mech.*, 424:217–241, 2000.

M. Quadrio, P. Ricco, and C. Viotti. Streamwise-traveling waves of spanwise wall velocity for turbulent drag reduction. *J. Fluid Mech.*, 627:161–178, 2009.

P. Ricco. Modification of near-wall turbulence due to spanwise wall oscillations. *J. Turbulence*, 5(24), 2004.

P. Ricco and M. Quadrio. Wall-oscillation conditions for drag reduction in turbulent channel flow. *Int. J. Heat Fluid Flow*, 29:601–612, 2008.

T. Segawa, H. Mizunuma, K. Murakami, F-C. Li, and H. Yoshida. Turbulent drag reduction by means of alternating suction and blowing jets. *Fluid Dyn. Res.*, 39:552–568, 2007.

L. Sirovich and S. Karlsson. Turbulent drag reduction by passive mechanisms. *Nature*, 388:753–755, 1997.

H. Tennekes and J.L. Lumley. *A First Course in Turbulence*. MIT Press, 1972.

M.J. Walsh. Drag characteristics of v-groove and transverse curvature riblets. *In Viscous Drag reduction (ed. G.R. Hough). American Institute of Aeronautics and Astronautics.*, 1980.

S. Xu, S. Dong, M.R. Maxey, and G.E. Karniadakis. Turbulent drag reduction by constant near-wall forcing. *J. Fluid Mech.*, 582:79–101, 2007.

A. Yakeno, Y. Hasegawa, and N. Kasagi. Spatio-temporally periodic control for turbulent friction drag reduction. In *Proc. 6th Int. Symp. on Turbulence and Shear Flow Phenomena TSFP6, Seoul.*, 2009.

H. Zhao, J.-Z. Wu, and J.-S. Luo. Turbulent drag reduction by traveling wave of flexible wall. *Fluid Dyn. Res.*, 34:175–198, 2004.